CHAPTER 6.

EXTERNAL PHOTON BEAMS: PHYSICAL ASPECTS

ERVIN B. PODGORSAK
Department of Medical Physics
McGill University Health Centre
Montréal, Québec, Canada

6.1. INTRODUCTION

Radiotherapy procedures fall into two main categories: *external beam radiotherapy* and *brachytherapy*. In external beam radiotherapy the radiation source is at a certain distance from the patient and the target within the patient is irradiated with an external radiation beam. In brachytherapy (see Chapter 13) radiation sources are placed directly into the target volume (intracavitary or interstitial brachytherapy) or onto a target (surface mold or intraoperative radiotherapy). Most of the external beam radiotherapy is carried out with photon beams, some with electron beams, and a very small fraction with more exotic particles, such as protons, heavier ions or neutrons.

This chapter deals with external photon beam radiotherapy. The photon external beams are all characterized by the same physical parameters but fall into various categories depending on their origin, means of production, and energy. With regard to the origin of photon beams we are dealing either with gamma rays that originate from radioactive nuclei or with x rays that originate in a target bombarded with energetic electrons. The x rays from a target consist of bremsstrahlung photons and characteristic photons. With regard to means of production the x rays are produced either in an x-ray tube (superficial or orthovoltage x rays) or in a linear accelerator (megavoltage x rays).

6.2. QUANTITIES USED IN DESCRIBING A PHOTON BEAM

Radiation dosimetry deals with two distinctly different entities: one describes the photon radiation beam itself in terms of the numbers and energies of photons constituting the photon beam and the other describes the amount of energy the photon beam may deposit in a given medium, such as air, water or biological material.

6.2.1. Photon fluence and photon fluence rate

- Photon fluence ϕ is defined as the quotient *dN* by *dA*, where *dN* is the number of photons that enter an imaginary sphere of cross-sectional area *dA*:

  $$\phi = \frac{dN}{dA} \qquad (6.1)$$

  The unit of ϕ is *photons*/cm^2.

- *Photon fluence rate* φ is defined as the photon fluence per unit time:

$$\varphi = \frac{d\phi}{dt} \quad , \tag{6.2}$$

with units of *photons* $\text{cm}^{-2} \cdot \text{s}^{-1}$.

6.2.2. Energy fluence and energy fluence rate

- *Energy fluence* ψ describes the energy flow in a photon beam and is defined as the amount of energy *dE* crossing a unit area *dA*:

$$\psi = \frac{dE}{dA} \tag{6.3}$$

with units MeV/cm^2.

- For a monoenergetic beam, *dE* is the number of photons *dN* times their energy $h\nu$, and the energy fluence in terms of photon fluence is:

$$\psi = \phi h\nu \tag{6.4}$$

- *Energy fluence rate* Ψ is defined as the energy fluence per unit time:

$$\Psi = \frac{d\psi}{dt} \quad , \tag{6.5}$$

with units $\text{MeV} \cdot \text{cm}^{-2} \cdot \text{s}^{-1}$.

6.2.3. Air-kerma in air

- For a monoenergetic photon beam in air, the air-kerma in air, $(K_{air})_{air}$, at a given point away from the source is proportional to the energy fluence ψ or photon fluence ϕ as follows:

$$(K_{\text{air}})_{\text{air}} = \psi \left(\frac{\mu_{\text{tr}}}{\rho}\right)_{\text{air}} = \phi\, h\nu \left(\frac{\mu_{\text{tr}}}{\rho}\right)_{\text{air}} \quad , \tag{6.6}$$

where $(\mu_{\text{tr}}/\rho)_{\text{air}}$ is the mass energy transfer coefficient for air at photon energy $h\nu$.

- Kerma K consists of two components: the *collision kerma* K^{col} and the *radiative kerma* K^{rad}, *i.e.*:

$$K = K^{\text{col}} + K^{\text{rad}} \quad . \tag{6.7}$$

- For monoenergetic photons in air the collisional kerma K^{col} is proportional to ψ and ϕ through the following relationships:

$$K^{\mathrm{col}} = \psi \left(\frac{\mu_{\mathrm{ab}}}{\rho}\right)_{\mathrm{air}} = h\nu\ \phi \left(\frac{\mu_{\mathrm{ab}}}{\rho}\right)_{\mathrm{air}} \quad , \tag{6.8}$$

where $(\mu_{\mathrm{ab}}/\rho)_{\mathrm{air}}$ is the mass energy absorption coefficient for air at photon energy $h\nu$. Often in the literature the energy absorption coefficient μ_{ab} is labelled as μ_{en}.

- The mass energy transfer coefficient (μ_{tr}/ρ) and mass energy absorption coefficient (μ_{ab}/ρ) are related through the following relationship:

$$\frac{\mu_{\mathrm{ab}}}{\rho} = \frac{\mu_{\mathrm{tr}}}{\rho}(1-g) , \tag{6.9}$$

whereg g is the bremsstrahlung fraction; *i.e.*, the fraction of the energy of secondary charged particles (electrons) that is lost to bremsstrahlung rather than being deposited in the medium. For low Z materials and photon energies below 1 MeV, the bremsstrahlung fraction $g \approx 0$; $(\mu_{\mathrm{tr}}/\rho) \approx (\mu_{\mathrm{ab}}/\rho)$, and $K \approx K^{\mathrm{col}}$.

6.2.4. Exposure in air

- The collisional air-kerma in air $(K_{\mathrm{air}}^{\mathrm{col}})_{\mathrm{air}}$ is related to exposure in air X through the following relationship:

$$(K_{\mathrm{air}}^{\mathrm{col}})_{\mathrm{air}} = X\ (W_{\mathrm{air}}/e) \quad , \tag{6.10}$$

where $(W_{\mathrm{air}}/\mathrm{e})$, as discussed in Section 9.1.3.) is the average energy required to produce an ion pair in dry air (33.97 eV/i.p.).

- The special unit of exposure is roentgen (R), while the SI unit is 2.58×10^{-4} C/kg with 1 R = 2.58×10^{-4} C/kg. Thus:

$$(K_{\mathrm{air}}^{\mathrm{col}})_{\mathrm{air}} = \left(2.58\times10^{-4}\ \frac{\mathrm{C}}{\mathrm{kg_{air}R}}\ 33.97\frac{\mathrm{J}}{\mathrm{C}}\right) X = \left[0.876\ \frac{\mathrm{cGy}}{\mathrm{R}}\right]\ X \quad , \tag{6.11}$$

with the exposure X given in rœntgens.

6.2.5. Dose to small mass of medium in air

The concept *"dose to small mass of medium in air"*, also known as *"dose in free space"*, was introduced by Johns and Cunningham to characterize the output of a radiation unit and to gain a reference dose for dosimetric calculations involving tissue-air-ratios and peak-scatter-factors. The "dose to small mass of medium in air" is designated as D'_{med} and is based on a measurement of the *air-kerma in air*. The concept has gained widespread use in orthovoltage and cobalt-60 therapy but is of limited use in megavoltage linac beam therapy.

The steps involved in determining the *"dose to small mass of medium in air"*, D'_{med}, at point P in a radiation beam from a signal M_P measured with an ionisation chamber centered at point P in air are:

$$M_P \xrightarrow{(1)} X_P \xrightarrow{(2)} (K_{\text{air}})_{\text{air}} \xrightarrow{(3)} (K_{\Delta\text{m}})_{\text{air}} \xrightarrow{(4)} (K_{\text{med}})_{\text{air}} \xrightarrow{(5)} D'_{\text{med}} \quad . \tag{6.12}$$

M_P is the signal measured with an ionisation chamber at point P and corrected for influence quantities, such as air temperature, air pressure, and recombination loss (see Section 9.3.). The ionisation chamber should have an appropriate build-up cap and an exposure calibration factor in air N_{x} or an air-kerma in air calibration factor N_{K}.

- *Step (1)*: Determine X_P, the exposure at point P, through:

  $$X_P = M_P \, N_{\text{X}} \quad . \tag{6.13}$$

- *Step (2)*: Determine $(K_{\text{air}})_{\text{air}}$, the *air-kerma in air* at point P through:

  $$(K_{\text{air}})_{\text{air}} = 0.876 \, \frac{\text{cGy}}{\text{R}} \, X_{\text{P}} \quad . \tag{6.14}$$

  Alternately, $(K_{\text{air}})_{\text{air}}$ may be determined from M_{P} directly, if N_{K} for the chamber is known, as follows:

  $$(K_{\text{air}})_{\text{air}} = M_{\text{P}} \, N_{\text{K}} \quad . \tag{6.15}$$

- *Step (3)*: Determine collision kerma to Δm, an infinitesimal mass of any other material (for example, water), in air from:

  $$(K_{\Delta\text{m}})_{\text{air}} = (K_{\text{air}})_{\text{air}} \left(\frac{\bar{\mu}_{\text{ab}}}{\rho} \right)_{\text{air}}^{\Delta m} \quad , \tag{6.16}$$

  where $\left(\bar{\mu}_{\text{ab}}/\rho\right)_{\text{air}}^{\Delta\text{m}}$ is the ratio of spectrum-averaged mass-energy absorption coefficients for Δm and air.

- *Step (4)*: Determine collision kerma to a spherical mass of medium centered around P and having a radius r_{med} just large enough to provide charged particle equilibrium at point P:

  $$(K_{\text{med}})_{\text{air}} = (K_{\Delta\text{m}})_{\text{air}} \, k(r_{\text{med}}) \quad , \tag{6.17}$$

  where $k(r_{\text{med}})$ is a correction factor accounting for the photon beam attenuation in the spherical mass of medium and approximated as:

  $$k(r_{\text{med}}) \approx e^{-\left(\frac{\mu_{\text{ab}}}{\rho}\right)_{\text{med}} \rho r_{\text{med}}} \quad , \tag{6.18}$$

where $(\mu_{ab}/\rho)_{med}$ is the mass-energy absorption coefficient for the medium and ρ the density of medium. For water, which is usually chosen as the medium, $k(r_{med}) \approx 0.985$ for cobalt-60 photons and approximately 1 for lower photon energies.

- *Step (5)*: "*Dose to small mass of medium in free space*", D'_{med}, is obtained from the following relationship:

$$D'_{med} = \beta\,(K_{med})_{air} = \beta\ 0.876\ \frac{\text{cGy}}{\text{R}} \left(\frac{\mu_{ab}}{\rho}\right)_{air}^{med} X_P\ k(r_{med}) \quad , \tag{6.19}$$

with β a proportionality constant equal to 1.003, 1.001, and 1.0 for cobalt-60, cesium-137, and x rays below 350 kVp, respectively. Often β is assumed equal to 1 even for cobalt-60 gamma rays.

- The product $0.876\ \frac{\text{cGy}}{\text{R}} \left(\frac{\mu_{ab}}{\rho}\right)_{air}^{med}$ is usually referred to as the *rœntgen-to-cGy conversion factor* f_{med} and the "*dose to small mass of medium in air*", assuming that $\beta \approx 1$, can then be written as:

$$D'_{med} = f_{med}\ X\ k(r_{med}) \quad . \tag{6.20}$$

6.3. PHOTON BEAM SOURCES

Photon sources are either isotropic or non-isotropic and they emit either monoenergetic or heterogeneous photon beams. The most common photon sources used in radiation oncology are: *x-ray machines*, *teletherapy isotope sources*, and *linear accelerators (linacs).*

- An isotropic photon source produces the same photon fluence rate in all directions, while the photon fluence rate from a non-isotropic source depends on direction of measurement.

- A plot of number of photons per energy interval vs. photon energy is referred to as photon spectrum. Sketches of photon spectra for a monoenergetic and a heterogeneous photon beam are given in Fig. 6.1(a) and (b), respectively. The area under curve (b) represents the total number of photons in the beam:

$$\phi = \int \frac{d\phi(h\nu)}{dh\nu}\ dh\nu \tag{6.21}$$

- All photons in a monoenergetic photon beam have the same energy $h\nu$ (Fig. 6.1(a)), while photons in a heterogeneous x-ray beam form a distinct spectrum with photons present in all energy intervals from 0 to a maximum value $h\nu_{max}$ which equals to the kinetic energy of electrons striking the target (Fig. 6.1(b)).

- In Fig. 6.1(b) the two spikes in the spectrum represent characteristic photons, while the continuous spectrum from 0 to $h\nu_{max}$ represents bremsstrahlung photons.

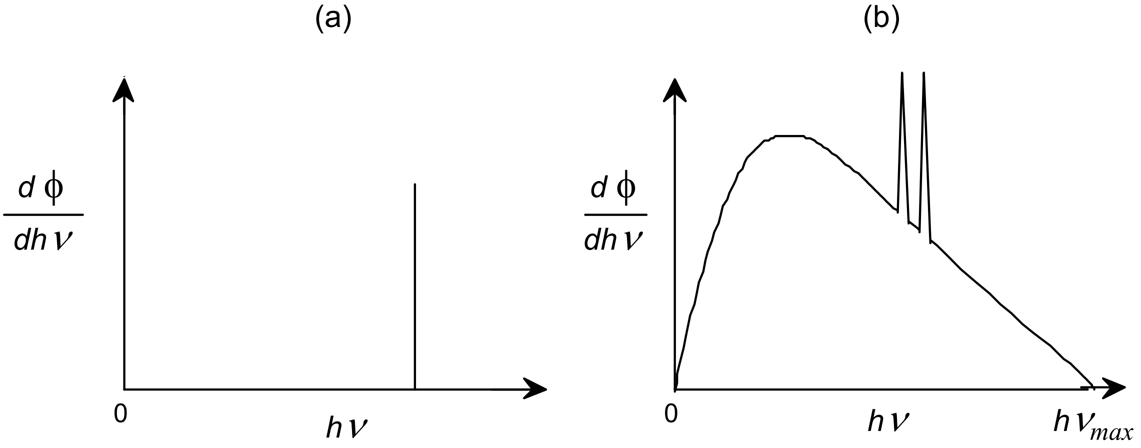

FIG. 6.1. Typical spectra for (a) monoenergetic and (b) heterogeneous photon beams.

- Gamma ray sources are usually isotropic and produce monoenergetic photon beams, while x-ray targets are non-isotropic sources producing heterogeneous photon spectra.

- Narrow monoenergetic photon beams will have identical first and second half-value layers (*HVL*s). In narrow heterogeneous photon beams, on the other hand, the second *HVL* will be either larger or smaller than the first *HVL*: larger in the superficial and orthovoltage range because of beam hardening effects and smaller in the high megavoltage range because of beam softening effects.

6.4. INVERSE SQUARE LAW

In external beam radiotherapy photon sources are often assumed to be point sources and the beams they produce are divergent beams, as shown schematically in Fig. 6.2. Let us assume that we have a photon point source *S* and a square field with side *a* (area $A = a^2$) at a distance f_a from the source. At a distance f_b we then get a square field with side *b* (area $B = b^2$), and the two fields are geometrically related as follows:

$$tg\,\beta = \frac{a/2}{f_a} = \frac{b/2}{f_b} \qquad \text{or} \qquad \frac{a}{b} = \frac{f_a}{f_b} \quad , \tag{6.22}$$

where β is the angle between the beam central axis and the geometric beam edge.

The photon source *S* emits photons and produces a photon fluence Φ_A at distance f_a and photon fluence Φ_B at distance f_b. Since the total number of photons N_{tot} crossing area *A* is equal to the total number of photons crossing area *B* (assuming no photon interactions take place in air between area *A* and area *B*), we can write:

$$N_{tot} = \phi_A A = \phi_B B \qquad \text{and} \qquad \frac{\phi_A}{\phi_B} = \frac{B}{A} = \frac{b^2}{a^2} = \frac{f_b^2}{f_a^2} \quad . \tag{6.23}$$

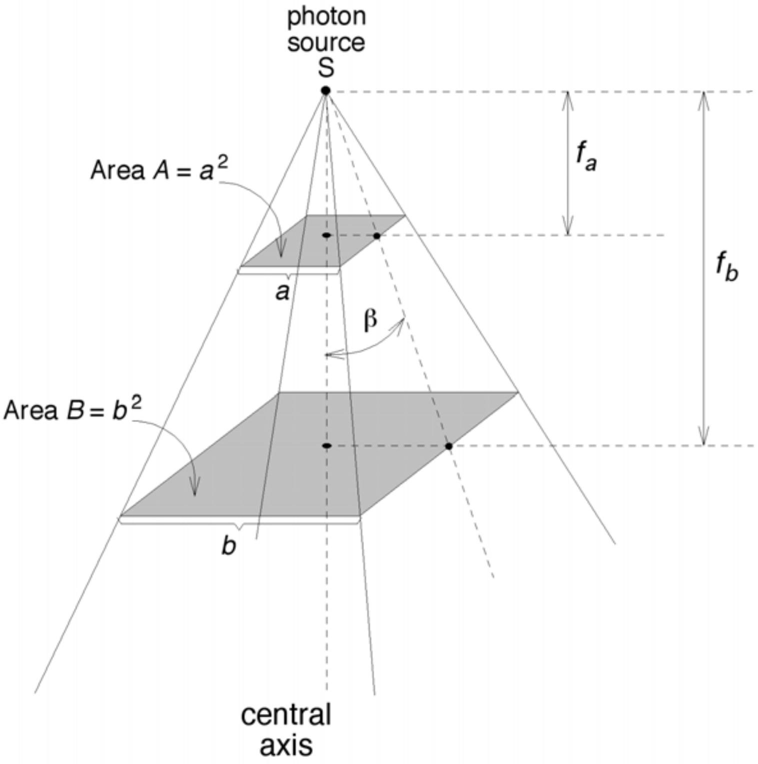

FIG. 6.2. Divergent photon beam originating in a photon point-source. At distance f_a from the source S the field size is $A = a^2$, at distance f_b the field size is $B = b^2$.

The photon fluence is thus inversely proportional to the square of the distance from the source. For example, if $f_b = 2f_a$ then the photon fluence at B will be exactly 1/4 of the photon fluence at A (*i.e.*, $\Phi_\text{B} = \Phi_\text{A} / 4$).

Since at a given point P in air the exposure in air X, *air-kerma in air* $\left(K_\text{air}\right)_\text{air}$, and "dose to small mass of medium in air" D'_med are directly proportional to the photon fluence at point P, it is reasonable to conclude that the three quantities: X, $\left(K_\text{air}\right)_\text{air}$, and D'_med all follow this inverse-square law behavior, *i.e.*:

$$\frac{X(f_a)}{X(f_b)} = \frac{\left(K_\text{air}(f_a)\right)_\text{air}}{\left(K_\text{air}(f_b)\right)_\text{air}} = \frac{D'_\text{med}(f_a)}{D'_\text{med}(f_b)} = \left(\frac{f_b}{f_a}\right)^2 \quad . \tag{6.24}$$

6.5. PENETRATION OF PHOTON BEAMS INTO A PHANTOM OR PATIENT

A photon beam propagating through air or vacuum is governed by the inverse-square law; a photon beam propagating through a phantom or patient, on the other hand, is not only affected by the inverse-square law but also by the attenuation and scattering of the photon beam inside the phantom or patient. The three effects make the dose deposition in a phantom or patient a complicated process and its determination a complex task.

A direct measurement of the dose distribution inside the patient is essentially impossible; yet, for a successful outcome of patient radiation treatment, it is imperative that the dose distribution in the irradiated volume be known precisely and accurately. This is usually achieved through the use of several functions which link the dose at any arbitrary point inside the patient to the known dose at the beam calibration (or reference) point in a phantom.

The functions are usually measured with suitable radiation detectors in tissue-equivalent phantoms and the dose or dose rate at the reference point is determined for, or in, water phantoms for a specific set of reference conditions, such as depth, field size, and source-surface distance, as discussed in detail in Chapter 9.

A typical dose distribution on the central axis of a megavoltage photon beam striking a patient is shown in Fig. 6.3. Several important points and regions may be identified. The beam enters the patient on the surface where it delivers a certain surface dose D_s. Beneath the surface the dose first rises rapidly, reaches a maximum value at depth $z_{\max}$ and then decreases almost exponentially until it reaches a value D_{ex} at the patient's exit point. The techniques for relative dose measurements are discussed in detail in Section 6.13.

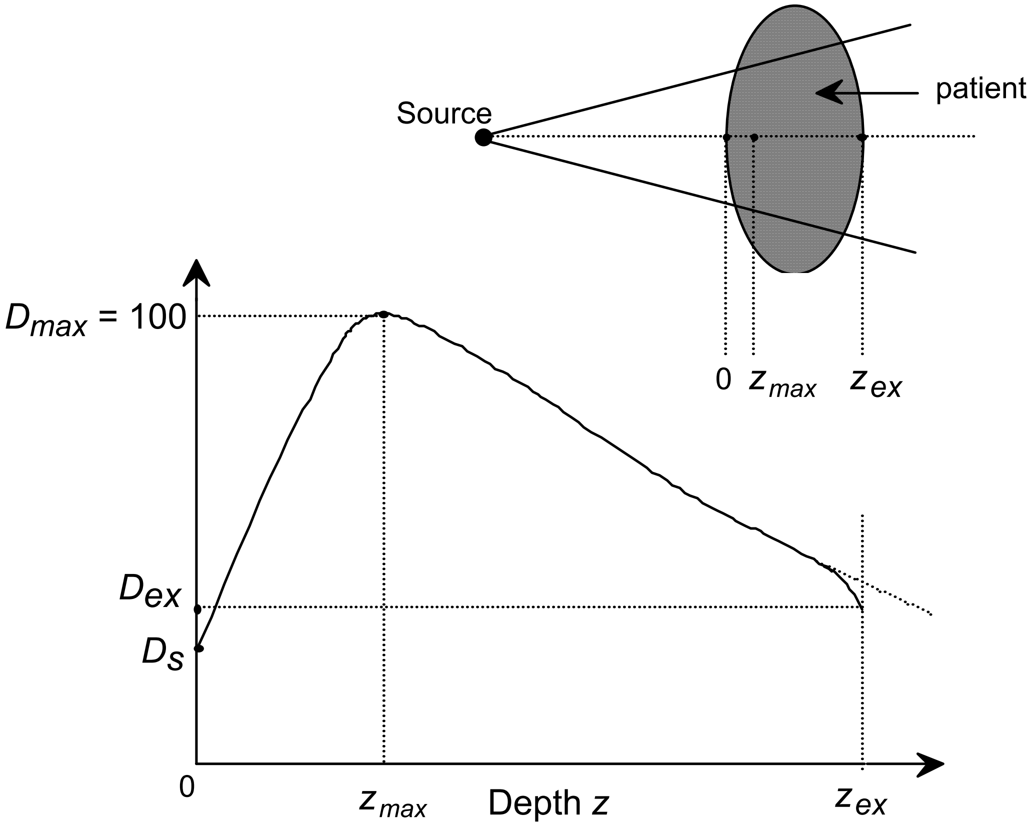

FIG. 6.3. Dose deposition in a patient from a megavoltage photon beam. D_s is the surface dose at the beam entrance side, D_{ex} is the surface dose at the beam exit side. D_{max} is the dose maximum often normalized to 100, resulting in a depth dose curve referred to as the percentage depth dose distribution. The region between $z = 0$ and $z = z_{\max}$ is referred to as the dose build-up region.

6.5.1. Surface dose

- For megavoltage photon beams the surface dose is generally much lower than the maximum dose which occurs at a depth $z_{\max}$ beneath the patient surface.

- In megavoltage photon beams the surface dose depends on beam energy and field size.

- The larger the photon beam energy, the lower is the surface dose, for a 10×10 cm^2 field typically amounting to some 30% of the maximum dose for a cobalt beam, 15% for a 6 MV x-ray beam and 10% for an 18 MV x ray beam. For a given beam energy the surface dose increases with field size.

- The low surface dose compared to the maximum dose is referred to as the *skin sparing effect* and represents an important advantage of megavoltage beams over orthovoltage and superficial beams in treatment of deep-seated tumours.

- Orthovoltage and superficial beams do not exhibit the skin sparing effect, since their dose maximum occurs on skin surface, *i.e.*, the surface dose is equal to the maximum dose.

- The surface dose is measured with thin window parallel-plate ionisation chambers for both chamber polarities, with the average reading between the positive and negative polarities taken as the surface dose value (see Section 6.13.).

- The surface dose represents contributions to the dose from:

  (1) Photons scattered from the collimators, flattening filter and air;
  (2) Photons backscattered from the patient; and
  (3) High-energy electrons produced by photon interactions in air and any shielding structures in the vicinity of the patient.

6.5.2. Buildup region

The dose region between the surface (depth $z = 0$) and depth $z = z_{\max}$ in megavoltage photon beams is referred to as the *dose buildup region* and results from the relatively long range of energetic secondary charged particles (electrons and positrons) that are first released in the patient by photon interactions (photoelectric effect, Compton effect, pair production) and then deposit their kinetic energy in the patient.

- In the region immediately beneath the patient surface, the condition of charged particle equilibrium (CPE) does not exist and the absorbed dose is much smaller than the collisional kerma. However, as the depth d increases, CPE is eventually reached at $z = z_{\max}$ where z is approximately equal to the range of secondary charged particles and the dose becomes comparable to the collision kerma.

- Beyond $z_{\max}$ both the dose and collisional kerma decrease because of the photon attenuation in the patient, resulting in a transient rather than true CPE.

6.5.3. Depth of dose maximum

The depth of dose maximum $z_{\max}$ beneath the patient surface depends on beam energy and beam field size. The beam energy dependence is the main effect; the field size dependence is often ignored because it represents only a minor effect.

- Nominal values for $z_{\max}$ range from 0 for superficial and orthovoltage x-ray beams, through 0.5 cm for cobalt-60 beams, to 5 cm for 25 MV beams, as shown in Table 6.I.

- For a given beam energy, the largest $z_{\max}$ occurs for fields of ~5×5 cm^2. For fields larger than 5×5 cm^2, $z_{\max}$ decreases because of collimator scatter effects; for fields smaller than 5×5 cm^2, $z_{\max}$ decreases because of phantom scatter effects.

6.5.4. Exit dose

The dose delivered to the patient at the beam exit point is referred to as the exit dose. As shown in Fig. 6.3, close to the beam exit point the dose distribution curves slightly downward from the extrapolated dose distribution curve. This relatively small effect is attributed to the missing scatter contribution at the exit point from points beyond the exit dose point. Similarly to the surface dose, the exit dose may be measured with a parallel-plate chamber, in this case with the chamber body oriented toward the source.

6.6. RADIATION TREATMENT PARAMETERS

External beam radiotherapy with photon beams is carried out with three types of treatment machines: x-ray units, isotope teletherapy units (mainly cobalt-60 units), and linear accelerators (linacs). The main parameters in external beam dose delivery with photon beams are: (i) depth of treatment, (ii) field size, (iii) source-surface distance in SSD setups or source-axis distance in *SAD* (isocentric) setups, and (iv) photon beam energy.

6.6.1. Radiation beam field size

Beams used for radiotherapy have various shapes that usually represent a compromise between the actual target shape and the need for simplicity and efficiency in beam shaping. Four general groups of field shapes are used: *square*, *rectangular*, *circular*, and *irregular*.

TABLE 6.I. TYPICAL DEPTHS OF DOSE MAXIMUM z_{max} FOR VARIOUS PHOTON BEAMS.

Beam energy	Superficial	Orthovoltage	Co-60	4 MV	6 MV	10 MV	18 MV	25 MV
$z_{\max}$ (cm)	0	0	0.5	1	1.5	2.5	3.5	5

Square and rectangular fields are usually produced with collimators installed in radiotherapy machines; circular fields with special collimators attached to the treatment machine; and irregular fields with custom-made shielding blocks or with multileaf collimators attached to a treatment machine.

- For any arbitrary radiation field an equivalent square or equivalent circular field may be found, meaning that the arbitrary field and the equivalent square field or equivalent circular field will be characterized with similar beam parameters and functions that are of importance in radiation dosimetry.

- An arbitrary rectangular field with sides a and b will be approximately equivalent to a square field with sides a_{eq} when both fields have the same area/perimeter ratio (Day's rule), *i.e.*,

$$\frac{ab}{2(a+b)} = \frac{a_{\mathrm{eq}}^{2}}{4a_{\mathrm{eq}}} \quad \text{or} \quad a_{\mathrm{eq}} = \frac{2ab}{a+b} \ . \tag{6.25}$$

- An arbitrary square field with sides a_{eq} will be equivalent to a circular field with radius r_{eq} when both fields have the same area, *i.e.,*

$$a_{\mathrm{eq}}^{2} = \pi r_{\mathrm{eq}}^{2} \quad \text{or} \quad r_{\mathrm{eq}} = \frac{a_{\mathrm{eq}}}{\sqrt{\pi}} \ . \tag{6.26}$$

6.6.2. Collimator factor

Exposure in air, air-kerma in air, and "dose to small mass of medium in air" at a given point P in air contain contributions from two components: *primary* and *scatter*.

- *Primary* is the major component; it comes directly from the source and does not depend on field size.

- *Scatter* represents a minor, yet non-negligible component; it consists of photons scattered into point P mainly from the collimator but also possibly from the air and the flattening filter of a linac. The scatter component depends on field size A (collimator setting): the larger the field size, the larger is the collimator surface available for scattering and consequently the larger is the scatter component.

- Exposure in air X, air-kerma in air $(K_{\mathrm{air}})_{\mathrm{air}}$ and "dose to small mass of medium in air" D'_{med} depend on field size A and a parameter referred to as the collimator factor CF (or collimator scatter factor S_{c} in Khan's notation or relative exposure factor REF in 1970s notation). The collimator factor is defined as: (6.27)

$$CF(A,h\nu) = S_{\mathrm{c}}(A,h\nu) = REF(A,h\nu) = \frac{X(A,h\nu)}{X(10,h\nu)} = \frac{\left(K_{\mathrm{air}}(A,h\nu)\right)_{\mathrm{air}}}{\left(K_{\mathrm{air}}(10,h\nu)\right)_{\mathrm{air}}} = \frac{D'(A,h\nu)}{D'(10,h\nu)}$$

- The geometry for the measurement of the collimator factor is shown in Fig. 6.4, in part (a) for the measurement of $D'(A,h\nu)$, in part (b) for the measurement of $D'(10,h\nu)$.

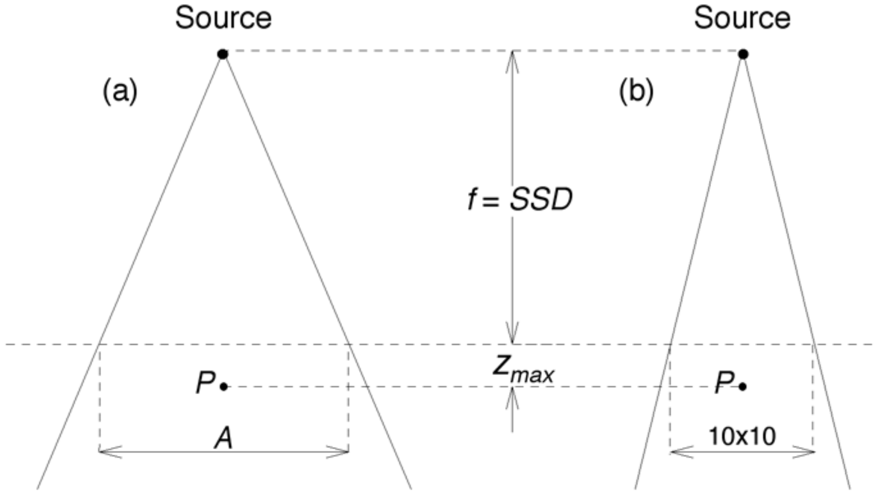

FIG. 6.4. Geometry for measurement of collimator factor CF(A, hν). The "dose to small mass of water" is measured at point P in air: in part (a) with field size A, in part (b) with field size 10×10 cm^2.

- The collimator factor is usually measured with an ionisation chamber with a build-up cap of a size large enough to provide maximum dose build-up for the given energy beam. For small fields one may carry out the measurements at large distances from the source so that the build-up cap is fully covered, however, the data are usually referred to the nominal *SSD* of the machine.

- Collimator factor is normalized to 1 for the nominal field of 10×10 cm^2 at the nominal *SSD* for the treatment machine. It is larger than 1 for fields *A* exceeding 10×10 cm^2 and smaller than 1 for fields *A* smaller than 10×10 cm^2. It is usually measured at point *P in air* with a cylindrical ionisation chamber equipped with an appropriate build-up cap and the chamber center placed at ($SSD + z_{\max}$) from the source. *SSD* here stands for the nominal source-surface distance (typically 80 or 100 cm for cobalt units and 100 cm for linacs) and $z_{\max}$ for the depth of dose maximum in phantom for the specific photon beam.

6.6.3. Peak scatter factor *PSF*

The "dose to small mass of medium" D'_P is measured with just enough material around the point of interest *P* to provide electronic equilibrium (ionisation chamber with appropriate build-up cap). D'_P is related to D_P, the dose at z_{max} in a phantom at point *P*, through the *peak-scatter factor PSF* as follows:

$$PSF\left(A, h\nu\right) = \frac{D_P(z_{\max}, A, f, h\nu)}{D'_P(A, h\nu)} \quad , \tag{6.28}$$

with the geometry shown in Fig. 6.5, for measurement of D'_P in part (a) and measurement of D_P in part (b). The chamber in part (a) is at a distance of $f + z_{\max}$ from the source.

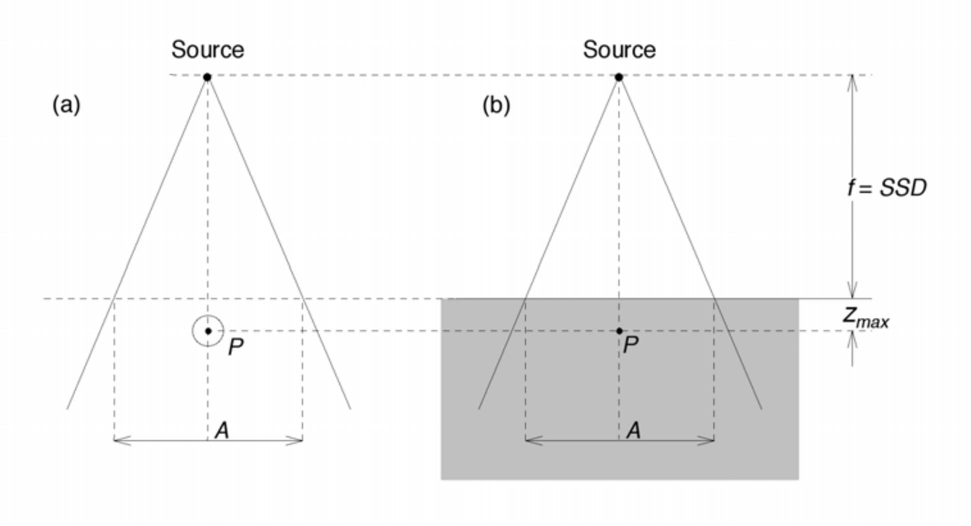

FIG. 6.5. Geometry for measurement of peak scatter factor PSF at point P.

At low photon energies $z_{\max} = 0$, point P is on the surface and the peak-scatter factor is referred to as the back-scatter factor. *PSF* depends on field size *A* as well as on photon beam energy $h\nu$, and gives the factor by which the radiation dose at point *P* in air is increased by radiation scattered to point *P* from the phantom or patient.

- Typical values for the *PSF* range from ~1 for small fields of megavoltage beams, through 1.054 for a 10×10 cm^2 field in a cobalt beam to 1.10 for a 50×100 cm^2 field in a cobalt beam (used for total body irradiation), to 1.50 for a 20×20 cm^2 field of orthovoltage x rays (*HVL* = 1 mm of copper).

- While backscattering is largest at very low photon energies (classical scattering), the energy of backscattered photons is small at low photon energies causing a rapid absorption of the scattered photons in the medium. At intermediate and high photon energies the backscattering and side-scattering decreases with energy; however, the scattered photons have a higher energy and larger penetrating power.

- The interrelationship between the amount of backscattering and scattered photon penetration causes the *PSF* first to increase with beam energy, reaching a peak around *HVL* ~ 1 mm of copper, and then decreasing with a further increase in beam energy. The beam quality at which maximum backscatter occurs depends on field size, shifting slightly toward harder radiation with increase in field size.

- For a given beam energy $h\nu$, the *PSF* increases with field size, as shown in Fig. 6.6 for a cobalt-60 beam.

- *Scatter factor SF* for field *A* is defined as the ratio:

$$SF\left(A,h\nu\right)=\frac{PSF(A,h\nu)}{PSF(10,h\nu)} \quad , \tag{6.29}$$

and thus represents the peak-scatter factor normalized to 1 for a 10×10 cm^2 field. In Khan’s notation the scatter factor is referred to as the phantom scatter factor and labeled as $S_p(A)$.

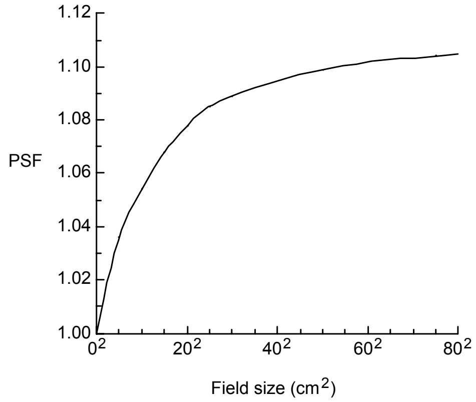

FIG.6.6. Peak scatter factor PSF as a function of field size for cobalt-60 gamma ray beam.

6.6.4. Relative dose factor *RDF*

For a given photon beam at a given source-surface distance, the dose at point *P* (at depth $z_{\max}$ in phantom) depends on the field size *A*; the larger the field size, the larger the dose. The *relative dose factor RDF* (referred to as the *total scatter factor* $S_{\mathrm{c,p}}$ in Khan's notation, or sometimes the machine output factor) is defined as the ratio of $D_P(z_{\max},A,f,h\nu)$, the dose at *P* in phantom for field *A* to $D_P(z_{\max},10,f,h\nu)$, the dose at *P* in phantom for a 10×10 cm^2 field:

$$RDF\left(A,h\nu\right)=S_{\mathrm{c,p}}\left(A,h\nu\right)=\frac{D_P\left(z_{\max},A,f,h\nu\right)}{D_P\left(z_{\max},10,f,h\nu\right)} \quad . \tag{6.30}$$

The geometry for measurement of the *RDF(A, hν)* is shown in Fig. 6.7, part (a) for the measurement of $D_P\left(z_{\max},A,f,h\nu\right)$, part (b) for the measurement of $D_P\left(z_{\max},10,f,h\nu\right)$.

- From the basic definitions of the collimator factor and the scatter factor we can write *RDF* as the following product:

$$\begin{aligned} RDF\left(A,h\nu\right)&=\frac{D_P\left(z_{\max},A,f,h\nu\right)}{D_P\left(z_{\max},10,f,h\nu\right)}= \\ &=\frac{D'_P\left(A,h\nu\right)\ PSF\left(A,h\nu\right)}{D'_P\left(10,h\nu\right)\ PSF\left(10,h\nu\right)}=CF\left(A,h\nu\right)\ SF\left(A,h\nu\right) \end{aligned} \tag{6.31}$$

  or in Khan's notation:

$$S_{\mathrm{c,p}}(A,h\nu)=S_{\mathrm{c}}(A,h\nu)\ S_{\mathrm{p}}(A,h\nu), \tag{6.32}$$

  indicating that the *RDF*(*A*) contains two components: scatter from the collimator and scatter from the phantom.

- Figure 6.8 shows typical values for the *RDF*(*A, hν*), *CF*(*A, hν*), and *SF(A, hν*) against field size *A* for a cobalt-60 beam. All three functions are normalized to 1 for *A* =10×10 cm^2; they are larger than 1 for *A* >10×10 cm^2 and smaller than 1 for *A* <10×10 cm^2.

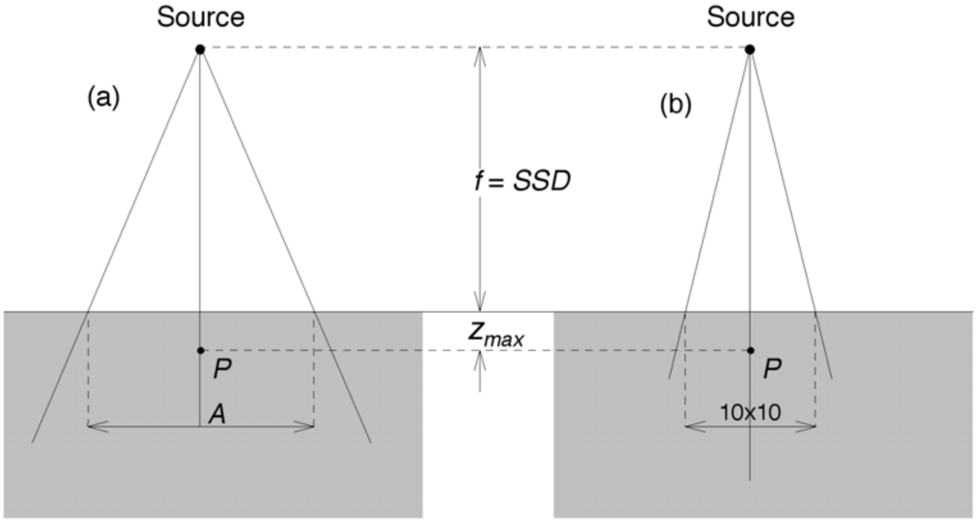

FIG. 6.7. Geometry for the measurement of the relative dose factor RDF(A). The dose at point P at $z_{\max}$ *in phantom is measured with field A in part (a) and with field* 10×10 *cm*^{2} *in part (b).*

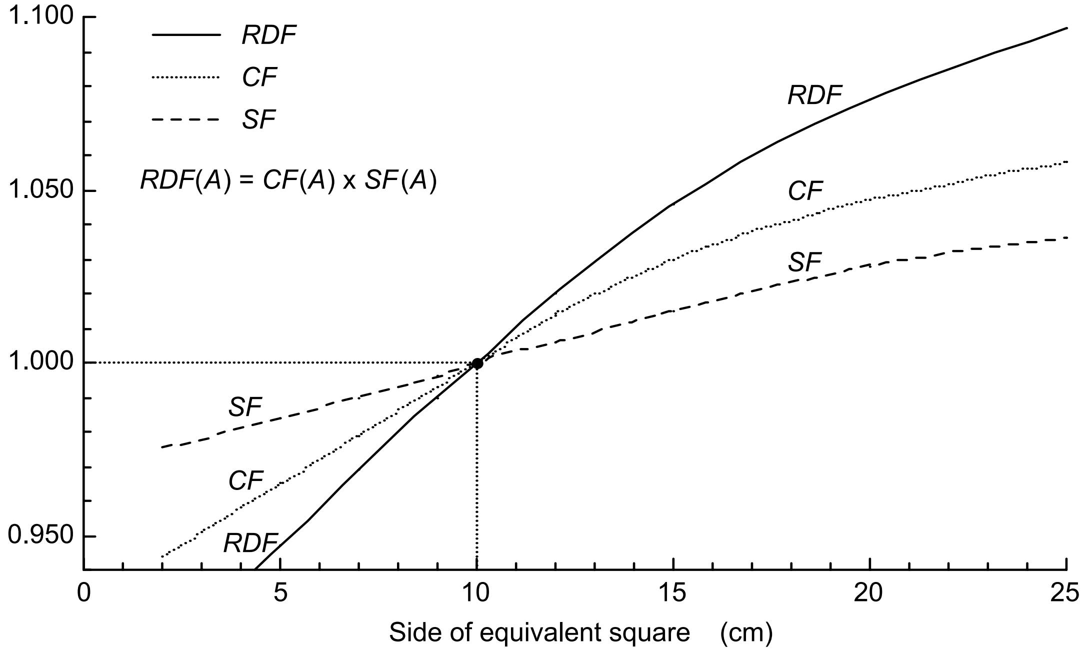

FIG. 6.8. Typical values for the relative dose factor RDF(A), collimator factor CF(A), and scatter factor SF(A) for a cobalt-60 gamma ray beam as a function of square field size A. All three functions are normalized to 1 *for a* 10×10 *cm*^{2}.

- When extra shielding is used on accessories tray or a multileaf collimator is used to shape the radiation field on patient's surface into an irregular field *B*, then the *RDF*(*B*, $h\nu$) is given as:

  $$RDF\left(B,h\nu\right)=CF\left(A,h\nu\right)\ SF\left(B,h\nu\right) \quad , \tag{6.33}$$

  where the field *A* represents the field set by the machine collimator and field *B* is the actual irregular field on the patient's surface.

6.7. CENTRAL AXIS DEPTH DOSES IN WATER: *SSD* SET-UP

6.7.1. Percentage depth dose

Central axis dose distributions inside the patient or phantom are usually normalized to D_{max} = 100% at the depth of dose maximum z_{max} and then referred to as the *percentage depth dose* distributions. The percentage depth dose is thus defined as follows:

$$PDD\left(d,A,f,h\nu\right)=100\ \frac{D_Q}{D_P}=100\frac{\dot{D}_Q}{\dot{D}_P} \quad , \tag{6.34}$$

where

D_Q and $\dot{D}_Q$ are the dose and dose rate at point Q at depth z on the central axis of the phantom;

D_P and $\dot{D}_P$ are the dose and dose rate at point P at $z_{\max}$ on the central axis of the phantom

The geometry for percentage depth dose definition is shown in Fig. 6.9. Point *Q* is an arbitrary point at depth *z* on the beam central axis; point *P* represents the specific dose reference point at $z = z_{max}$ on the beam central axis. *PDD* depends on four parameters: depth in phantom *d*, field size *A*, source-surface distance $SSD = f$ and photon beam energy $h\nu$. *PDD* ranges in value from 0 at $z \to \infty$ to 100 at $z = z_{max}$.

- The dose at point *Q* contains two components: primary and scatter.
  - The primary component may be expressed as:

    $$PDD^{\text{pri}}=100\ \frac{D_Q^{\text{pri}}}{D_P^{\text{pri}}}=\left(\frac{f+z_{\max}}{f+z}\right)^2 e^{-\mu_{\text{eff}}\left(z-z_{\max}\right)} \quad , \tag{6.35}$$

    where μ_{eff} is the linear attenuation coefficient for the primary beam in the phantom material (μ_{eff} for a cobalt-60 beam in water is 0.0657 cm^{-1}).
  - The scatter component reflects the relative contribution to point *Q* of scattered radiation.

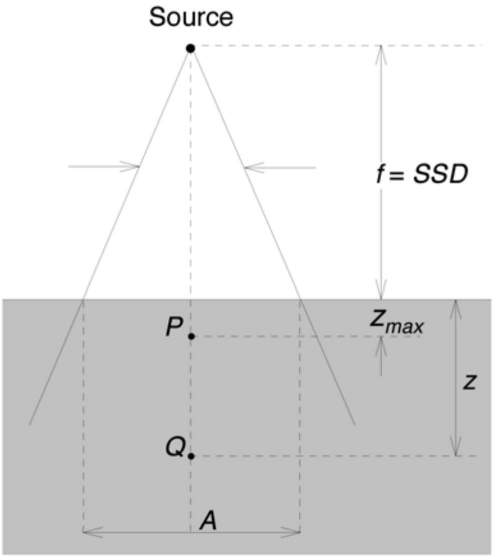

FIG. 6.9. Geometry for percentage depth dose measurement and definition. Point Q is an arbitrary point on the beam central axis at depth d, point P is the point at z_{max} *on the beam central axis. The field size A is defined on the surface of the phantom.*

- As sketched in Fig. 6.3, for a constant A, f and $h\nu$, *PDD* first increases from the surface to $z = z_{max}$ and then decreases with a further increase in z. The depth of dose maximum as well as the surface dose depends on the beam energy; the larger the beam energy, the larger is the depth of dose maximum and the lower is the surface dose.

- For constant z, f and $h\nu$, the *PDD* increases with increasing A because of increased scatter contribution to points on the central axis. An example for a cobalt-60 beam is given in Table 6.II.

- For constant z, A and $h\nu$, the *PDD* increases with increasing f because of a decreasing effect of z on the inverse-square factor which governs the primary component of the photon beam. An example for a cobalt-60 beam is given in Table 6.III.

- For constant z, A and f, the *PDD* beyond $z_{\max}$ increases with beam energy, because of a decrease in beam attenuation, *i.e.*, because of an increase in beam penetrating power.

- An example of *PDD* distributions for 10×10 cm^2 fields and various megavoltage photon beams is given in Fig. 6.10 and Table 6.IV. The size of the build-up region increases with beam energy and the surface dose decreases with beam energy.

- Percentage depth doses for radiotherapy beams are usually tabulated for square fields; however, the majority of fields used in radiotherapy are rectangular or shaped irregularly. The concept of equivalent squares is used to determine the square field that will be equivalent to the given rectangular or irregular field.

TABLE 6.II. PERCENTAGE DEPTH DOSES FOR A COBALT-60 BEAM IN WATER FOR VARIOUS FIELD SIZES AND AN *SSD* OF 100 cm.

A (cm^2)	0×0	5×5	10×10	15×15	20×20	25×25	50×50
PDD (5,A,100,Co)	68.2*	76.7	80.4	82.0	83.0	83.4	85.2
PDD (10,A,100,Co)	44.7*	53.3	58.7	61.6	63.3	64.4	67.3
PDD (15,A,100,Co)	29.5*	36.5	41.6	44.9	47.1	48.6	49.7

* Calculated using Eq. (6.35) with $\mu = 0.0657\ \text{cm}^{-1}$.

TABLE 6.III. PERCENTAGE DEPTH DOSES FOR A COBALT-60 BEAM IN WATER FOR VARIOUS SOURCE-SURFACE DISTANCES, DEPTH *z* OF 5 cm IN PHANTOM AND A FIELD OF A = 10×10 cm^2.

f = SSD (cm)	60	80	100	120	140
PDD (5,10,f,Co)	76.2	78.8	80.0	81.3	82.3

TABLE 6.IV. PERCENTAGE DEPTH DOSES FOR VARIOUS PHOTON BEAMS IN WATER PHANTOM WITH A FIELD SIZE *A* OF 10×10 cm^2, *SSD* OF 100 cm AND TWO DEPTHS: 5 cm AND 10 cm.

Photon beam $h\nu$	Co-60	4 MV	6 MV	10 MV	18 MV	25 MV
Nominal z_{max} *(cm)*	0.5	1.0	1.5	2.5	3.5	5.0
PDD (5,10,100, $h\nu$*)*	80	84	86	92	97	98
PDD (10,10,100, $h\nu$*)*	59	65	67	74	80	82

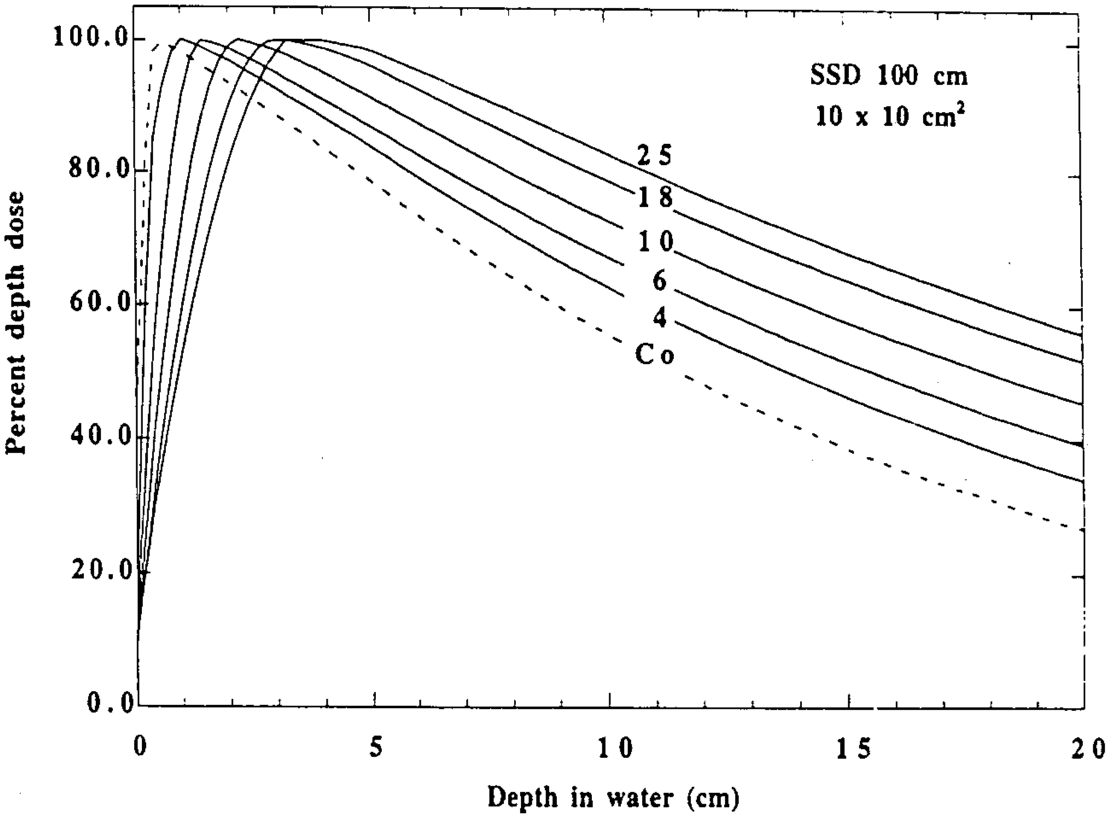

FIG. 6.10. Percentage depth dose curves in water for a 10×10 cm² field at an SSD of 100 cm for various megavoltage photon beams ranging from cobalt-60 gamma rays to 25 MV x rays.

6.7.2. Scatter function S

In radiation dose calculations it is often desirable to separate the scatter component from the total dose at Q, *i.e.*:

Scatter component at Q = Total dose at Q – Primary dose at Q =

$$= D'_P \; PSF(A,h\nu) \; PDD(z,A,f,h\nu) - D'_P \; PSF(0,h\nu) \; PDD(z,0,f,h\nu) \; . \tag{6.36}$$

The *scatter function* $S(z,A,f,h\nu)$ is then defined as:

$$S(z,A,f,h\nu) = PSF(A,h\nu) \; PDD(z,A,f,h\nu) - PSF(0,h\nu) \; PDD(z,0,f,h\nu) , \tag{6.37}$$

giving the scatter dose at point Q per 100 cGy of primary dose at point P. Note: $PSF(0) = 1$ and $PDD(z,0,f,h\nu)$ is the primary PDD calculated with Eq. (6.35).

Similarly to PDD, the scatter function S also depends on four parameters: depth z, field size A, source-surface distance f, and beam energy $h\nu$.

- For constant A, f, and $h\nu$, the scatter function S first increases with z, reaches a peak, and then slowly decreases with a further increase in z.
- For constant z, f, and $h\nu$, S increases with field size A.
- At $z = z_{\max}$ the scatter function S is given by:

$$S\left(z_{\max}, A, f, h\nu\right) = 100\left[PSF\left(A, h\nu\right) - 1\right] \tag{6.38}$$

6.8. CENTRAL AXIS DEPTH DOSES IN WATER: *SAD* SET-UP

When multiple fields are used for treatment of a particular tumour inside the patient, isocentric (*SAD*) setups are often used because they are more practical in comparison with constant *SSD* setups. Most megavoltage units are mounted isocentrically with an *SAD* of 80 cm or more commonly 100 cm to allow this treatment option. In contrast to SSD setups which rely on *PDD* distributions, *SAD* setups rely on other functions, such as tissue-air ratios and tissue-phantom ratios, for dosimetric calculations.

6.8.1. Tissue-air ratio $TAR(z, A_Q, h\nu)$

Tissue-air ratio $TAR(z,A_Q,h\nu)$ was originally introduced by Johns to simplify dose calculations in rotational radiotherapy, but its use was subsequently expanded to isocentric irradiations with multiple stationary fields. In rotational radiotherapy the radiation source moves in a circle around the axis of rotation that is usually placed inside the tumour. During the rotation around the patient the *SSD* varies with the patient contour; however, source-axis distance remains constant.

$TAR(z,A_Q,h\nu)$ is defined as the ratio of the dose D_Q at point Q on the central axis in the patient or phantom to the dose D'_Q, the "dose to small mass of water in air" at the same point Q on the beam central axis:

$$TAR\left(z, A_Q, h\nu\right) = \frac{D_Q}{D'_Q} \quad . \tag{6.39}$$

The geometry for *TAR* measurement is shown in Fig. 6.11; part (a) for measurement of D_Q in phantom and part (b) for measurement of D'_Q in air. The field size A_Q is defined at point Q that is normally placed into the isocenter of the treatment machine.

In contrast to the PDD($z,A,f,h\nu$) which depends on four parameters, the TAR($z,A_Q,h\nu$) depends only on three: depth z, field size A_Q at depth z, and beam energy $h\nu$; there is essentially no *SSD* or *SAD* dependence in the range of *SSD*s used clinically (50-150 cm). Tissue-air ratios for various cobalt-60 beams at depths of 5 cm and 10 cm in water are given in Table 6.V.

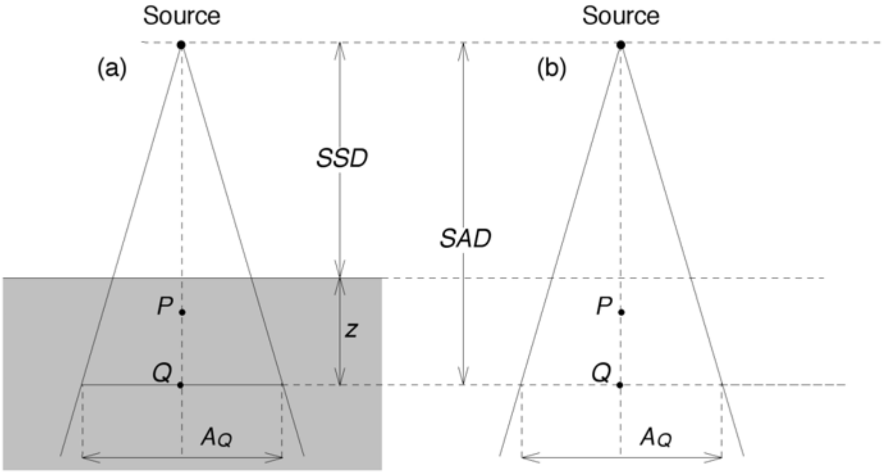

FIG. 6.11. Geometry for measurement and definition of tissue-air ratio. In part (a) the dose is determined at point Q in a water phantom, in part (b) the "dose to small mass of water" is determined at point Q. Point Q is at the machine isocenter at a distance SAD from the source. The beam field size A_Q is defined at depth d in the phantom.

- For constant A_Q and $h\nu$, the *TAR* decreases with an increasing z beyond z_{max}.
- For constant z and $h\nu$, the *TAR* increases with increasing A_Q.
- For constant z and A_Q, the *TAR* increases with $h\nu$.
- For $z = z_{\max}$, the *TAR* becomes identical to the *PSF*:

$$TAR\left(z = z_{\max}, A_Q = A_P, h\nu\right) = PSF\left(A_P, h\nu\right) \quad . \tag{6.40}$$

- The zero area *TAR*, *i.e.*, $TAR(z, 0, h\nu)$, may be calculated from:

$$TAR\left(z, 0, h\nu\right) = e^{-\mu_{eff}\left(z - z_{\max}\right)} \quad , \tag{6.41}$$

  where μ_{eff} is the effective attenuation coefficient for the photon beam $h\nu$. A 0×0 field is a hypothetical field in which the dose at depth in phantom is entirely due to primary photons since the volume that can scatter radiation is zero.

- Tissue-air ratios are most reliably measured with ionisation chambers; however, the measurements are much more cumbersome than those of measurement of percentage depth doses. In the case of *TAR*s the depth in water must be measured in such a way that the distance between the ionisation chamber and radiation source remains constant and this is difficult to achieve using automatic techniques. Moreover, the measurement of the "dose to small mass of water" must be carried out with great care to ensure full build-up and readings free of radiation scattered into the chamber from treatment room walls or floor.

TABLE 6.V. TISSUE-AIR RATIOS FOR A COBALT-60 BEAM IN WATER FOR VARIOUS FIELD SIZES A_Q AND TWO DEPTHS IN PHANTOM: 5 cm AND 10 cm.

A_Q (cm^2)	0×0	5×5	10×10	15×15	20×20	25×25
$TAR(5,A_Q,Co)$	0.744*	0.864	0.921	0.953	0.974	0.986
$TAR(10,A_Q,Co)$	0.536*	0.654	0.731	0.779	0.809	0.831

* Calculated using Eq. (6.41) with $\mu = 0.0657$ cm^{-1}.

Since the concept of “dose to small mass of medium” is not recommended for use with megavoltage beams above cobalt-60 and 4 MV, the concept of *TAR* is not used in dosimetry of medium and high energy photon beams. For these energies functions are used that are similar to the *TAR* but do not suffer the limitations imposed on the measurement of the “dose to small mass of medium”.

6.8.2. Relationship between $TAR(d,A_Q,h\nu)$ and $PDD(d,A,f,h\nu)$

As sketched in Fig. 6.12, a simple relationship may be derived between $TAR(z,A_Q,h\nu)$ and the corresponding $PDD(z,A,f,h\nu)$ from the basic definitions governing the two functions. The basic definitions for the two functions are:

$$TAR(z,A_Q,h\nu) = \frac{D_Q}{D'_Q} \quad , \tag{6.42}$$

$$PDD(z,A,f,h\nu) = 100\,\frac{D_Q}{D_P} \quad , \tag{6.43}$$

and solving Eqs. (6.42) and (6.43) for D_Q we get:

$$D_Q = D_P\,\frac{PDD(z,A,f,h\nu)}{100} = D'_Q\,TAR(z,A_Q,h\nu) \quad . \tag{6.44}$$

D_P may now be written as:

$$D_P = D'_P\,PSF(A,h\nu) = D'_Q\left(\frac{f+z}{f+z_{\max}}\right)^2 PSF(A,h\nu) \tag{6.45}$$

and inserted into Eq. (6.44) to yield:

$$TAR(z,A_Q,h\nu) = PSF(A,h\nu)\,\frac{PDD(z,A,f,h\nu)}{100}\left(\frac{f+z}{f+z_{\max}}\right)^2 \quad . \tag{6.46}$$

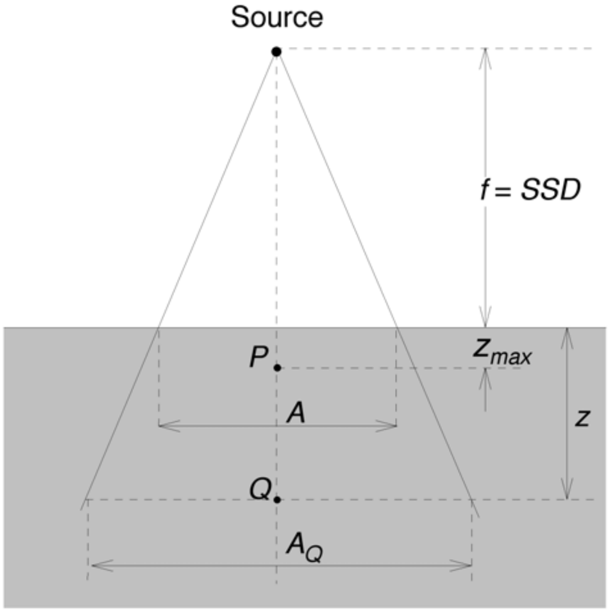

FIG. 6.12. Geometry for the relationship between PDD(z,A,f, hν) and TAR(z,A$_Q$, hν).

- For a special case of $z = z_{\max}$ where $PDD(z_{\max}, A, f, h\nu) = 100$, Eq. (6.46) above shows that the *PSF(A, hν)* is a special $TAR(z_{\max}, A, h\nu)$. The range of *TARs* is therefore from 0 at $z \to \infty$ to $PSF(A, h\nu)$ at $z = z_{\max}$.

- Since *TAR* does not depend on *SSD*, a single *TAR* table for a given photon beam energy may be used to cover all possible *SSD*s used clinically.

- Alternatively, *PDDs* for any arbitrary combination of *z*, *A*, and *f* = *SSD* may be calculated from a single *TAR* table.

- Based on Eq. (6.46) we derive the following two relationships for *PDDs* at two different *SSDs* (f_1 and f_2).

  - The first relationship assumes an identical field size *A* at the two *SSDs*, as shown in Fig. 6.13:

$$\frac{PDD(z, A, f_1, h\nu)}{PDD(z, A, f_2, h\nu)} = \left\{\frac{TAR(z, A_{Q_1}, h\nu)}{TAR(z, A_{Q_2}, h\nu)}\right\} \left\{\frac{\dfrac{f_1 + z_{\max}}{f_1 + z}}{\dfrac{f_2 + z_{\max}}{f_2 + z}}\right\}^2 . \qquad (6.47)$$

  - The second relationship assumes the same field size A_Q at depth *z* at the two *SSD*s, as shown in Fig. 6.14:

$$\frac{PDD(z, A_1, f_1, h\nu)}{PDD(z, A_2, f_2, h\nu)} = \left\{\frac{PSF(A_2, h\nu)}{PSF(A_1, h\nu)}\right\} \left\{\frac{\dfrac{f_1 + z_{\max}}{f_1 + z}}{\dfrac{f_2 + z_{\max}}{f_2 + z}}\right\}^2 . \qquad (6.48)$$

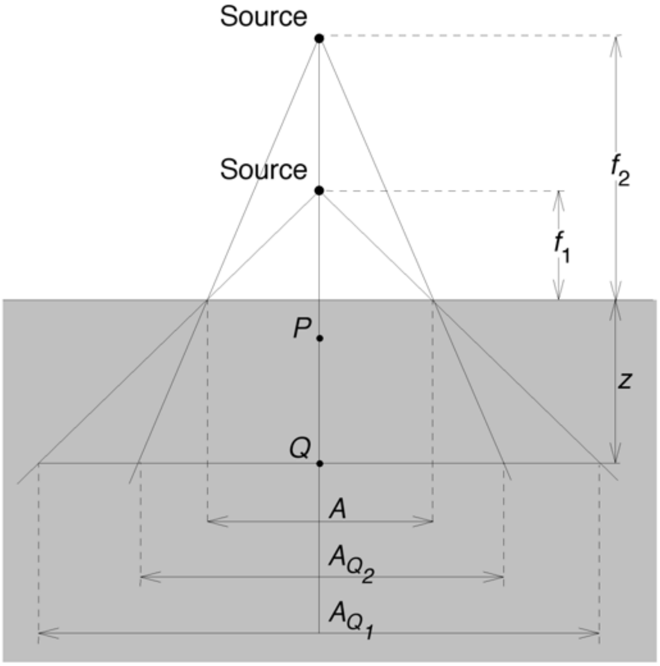

FIG. 6.13. Derivation of the PDD relationship for two SSDs with field size A identical for both. Note that the field A on the phantom surface is the same for both SSD; therefore the fields at depth d differ for the two SSDs but are related through simple geometrical relationships.

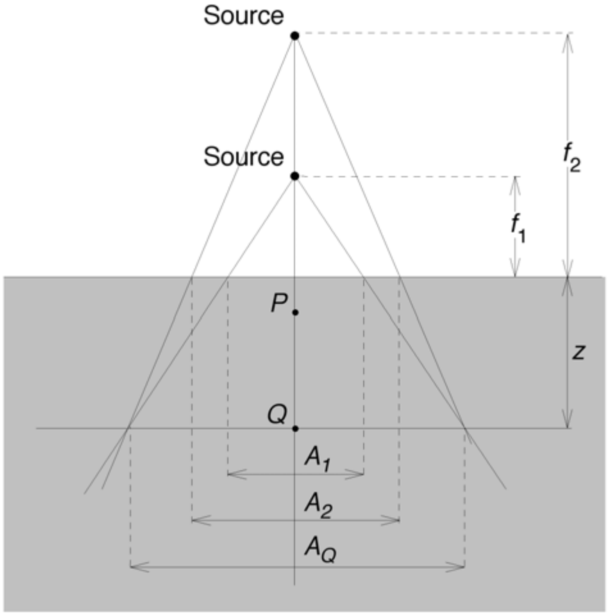

FIG. 6.14. Derivation of the PDD relationship for two SSDs with field size A_Q equal for both. Here the fields A_1 and A_2 on the phantom surface are related through simple geometrical relationships.

- The relationships in Eq. (6.47) and Eq. (6.48) consist of two components each; the inverse-square law correction component is the main component of the correction and it is referred to as the Mayneord factor. The second factor, represented by the ratio of *TAR*s or *PSF*s, is often ignored, because its effect is much smaller than that produced by the Mayneord factor. Then the Mayneord factor alone is used for correction of *PDDs* from one *SSD* to another.

6.8.3. Scatter-air ratio $SAR(z,A_Q,h\nu)$

Just as it was convenient in dealing with percentage depth doses to separate out the scattered component from the primary component to get the scatter function, it is sometimes useful to separate the primary component of *TAR* from the total *TAR* to get the scatter contribution which, in this case, is referred to as the scatter-air ratio $SAR(d,A_Q,h\nu)$. It is defined as:

$$SAR\left(z,A_Q,h\nu\right)=TAR\left(z,A_Q,h\nu\right)-TAR\left(z,0,h\nu\right) \quad , \tag{6.49}$$

depends on the same three parameters as the *TAR*, and gives the scatter contribution to the dose at point *Q* in phantom per 1 cGy of dose to small mass of water at point *Q* in air.

6.8.4. Relationship between $SAR(z,A_Q,h\nu)$ and $S(z,A,f,h\nu)$

Similarly to the relationship between $TAR(z,A_Q,h\nu)$ and $PDD(z,A,f,h\nu)$, we can derive the relationship between $SAR(z,A_Q,h\nu)$ and $S(d,A,f,h\nu)$ to get:

$$SAR(z,A_Q,h\nu)=\frac{S(z,A,f)}{100}\left(\frac{f+z}{f+z_{\max}}\right)^2 \quad . \tag{6.50}$$

It is easy to see that:

$$S(z,A,f,h\nu)=100\;SAR(z,A_Q,h\nu) \tag{6.51}$$

for any z when $f\rightarrow\infty$ and for any f when $z\rightarrow z_{\max}$.

6.8.5. Tissue-phantom ratio $TPR(z,A_Q,h\nu)$ and tissue-maximum ratio $TMR(z,A_Q,h\nu)$

The *TAR* concept works well in isocentric setups for photon energies of cobalt-60 and below. For megavoltage x rays produced by high energy linacs, however, the concept breaks down, because of difficulties in measuring the "dose to small mass of water in air" at those energies (the size of the required buildup cap for the ionisation chamber becomes excessively large). To bypass this problem, the concept of tissue-phantom ratio *TPR* was introduced for use in megavoltage isocentric setups.

The *TPR* is defined as follows:

$$TPR(z, A_Q, h\nu) = \frac{D_Q}{D_{Q_{ref}}} = \frac{\dot{D}_Q}{\dot{D}_{Q_{ref}}} \quad , \tag{6.52}$$

where

D_Q and $\dot{D}_Q$ are the dose and dose rate, respectively, in phantom at arbitrary point Q on the beam central axis and

$D_{Q_{ref}}$ and $\dot{D}_{Q_{ref}}$ are the dose and dose rate, respectively, in phantom at a reference depth d_{ref} (typically 5 or 10 cm) on the beam central axis.

The geometry for the measurements of doses D_Q and $D_{Q_{ref}}$ is shown in Fig. 6.15.

A special *TPR* was defined for the reference depth z_{ref} equal to the depth of dose maximum z_{max} and it is referred to as the tissue-maximum ratio $TMR(z, A_Q, h\nu)$:

$$TMR(z, A_Q, h\nu) = \frac{D_Q}{D_{Q_{max}}} = \frac{\dot{D}_Q}{\dot{D}_{Q_{max}}} \quad , \tag{6.53}$$

where

D_Q and $\dot{D}_Q$ are the dose and dose rate, respectively, at point Q at a depth z in phantom

$D_{Q_{max}}$ and $\dot{D}_{Q_{max}}$ are the dose and dose rate, respectively, at point Q at z_{max}.

The geometry for the definition of *TMR* is the same as in Fig. 6.15 except that z_{ref} is now z_{max}

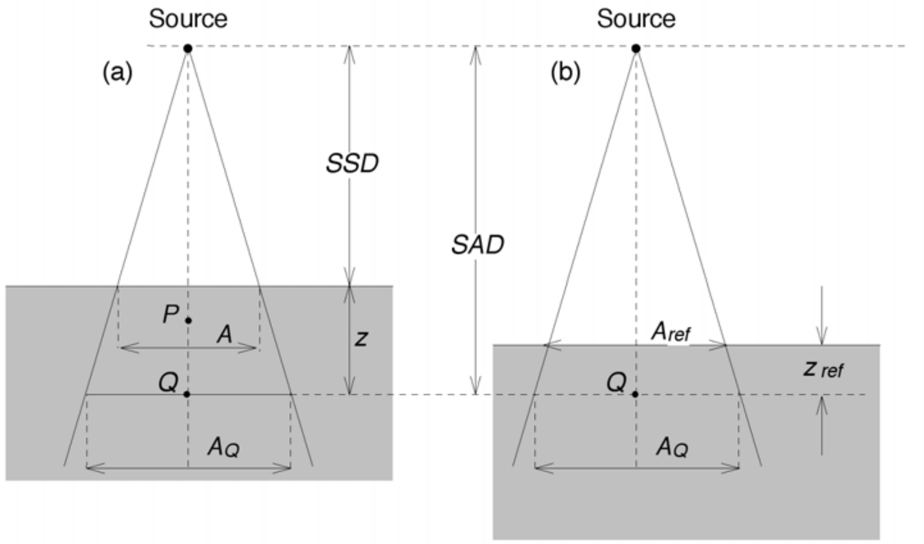

FIG. 6.15. Geometry for measurement of tissue-phantom ratio $TPR(d, A_Q, h\nu)$

- Just like the *TAR*, the *TPR* and *TMR* depend on three parameters: z, A_Q, $h\nu$ but do not depend on the *SAD* or *SSD*.
- The range of *TMR* is from 0 for $z \rightarrow \infty$ to 1 for $z = z_{\max}$, i.e., $0 \le TMR(z, A_Q, h\nu) \le 1$.
- For constant A_Q and $h\nu$, the *TMR* decreases with increasing z.
- For constant z and $h\nu$, the *TMR* increases with increasing A_Q.
- For constant z and A_Q, the *TMR* increases with increasing $h\nu$.

6.8.6. Relationship between $TMR(z,A_Q,h\nu)$ and $PDD(z,A,f,h\nu)$

As sketched in Fig. 6.16, a simple relationship may be derived between the $TMR(\mathrm{d},A_Q,h\nu)$ and the corresponding $PDD(d,A,f,h\nu)$ from the basic definitions governing the two functions. The basic definitions for the two functions are:

$$TMR(z, A_Q, h\nu) = \frac{D_Q}{D_{Q_{\max}}} \quad , \tag{6.54}$$

$$PDD(z, A, f, h\nu) = 100\ \frac{D_Q}{D_P} \quad . \tag{6.55}$$

Solving Eqs. (6.54) and (6.55) for D_Q we get:

$$D_Q = D_P \frac{PDD(z, A, f, h\nu)}{100} = D_{Q_{\max}}\ TMR(z, A_Q, h\nu) \quad , \tag{6.56}$$

and expanding D_P and $D_{Q_{\max}}$ as follows:

$$D_P = D_P'\ PSF(A, h\nu) = D_Q' \left(\frac{f+z}{f+z_{\max}} \right)^2 PSF(A, h\nu) \tag{6.57}$$

$$D_{Q_{\max}} = D_Q'\ PSF\left(A_Q, h\nu\right) \tag{6.58}$$

we obtain:

$$TMR(z, A_Q, h\nu) = \frac{PDD(z, A_Q, h\nu)}{100}\ \frac{PSF(A, h\nu)}{PSF(A_Q, h\nu)} \left(\frac{f+z}{f+z_{\max}} \right)^2 \quad . \tag{6.59}$$

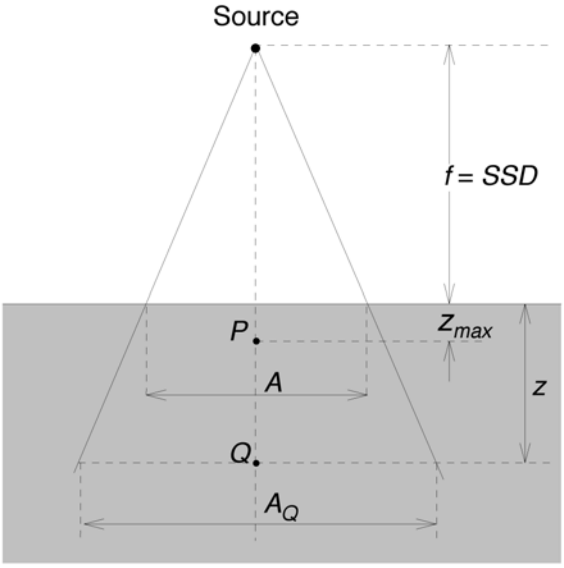

FIG. 6.16. Geometry for derivation of relation between PDD(z,A,f, hν) and TMR(z,A_Q, hν).

In the first approximation, ignoring the *PSF* ratio in Eq. (6.59), we get a very simple approximate relationship between *TMR(z,A_Q, hν)* and *PDD(z,A,f, hν)* as:

$$TMR\left(z,A_Q,h\nu\right) \approx \frac{PDD\left(z,A,f,h\nu\right)}{100}\left(\frac{f+z}{f+z_{\max}}\right)^2 . \tag{6.60}$$

The error in ignoring the ratio $PSF(A,h\nu)/PSF(A_Q,h\nu)$ is very small and can be estimated easily for a cobalt beam. For an extreme example, take the case with depth in phantom d = 20 cm, field size $A = 20\times20$ cm^2, and source-surface distance f = 100 cm to get $A_Q = 24\times24$ cm^2 and *PSF*(20,Co)/*PSF*(24,Co) = 1.078/1.083 = 0.995 or a 0.5% error. Errors for smaller fields and shorter *SSD*s are obviously smaller, making Eq. (6.60) a reasonable and very practical approximation.

6.8.7. Scatter-maximum ratio $SMR(z,A_Q,h\nu)$

Similarly to separating the tissue-air ratio $TAR(z,A_Q,h\nu)$ into the primary component $TAR(z,0,h\nu)$ and the scatter component (scatter-air ratio) $SAR(z,A_Q,h\nu)$, the tissue-maximum ratio $TMR(z,A_Q,h\nu)$ can be separated into the primary component $TMR(z,0,h\nu)$ and the scatter component referred to as the scatter-maximum ratio $SMR(z,A_Q,h\nu)$. The scatter-maximum ratio is thus defined as follows:

$$SMR(z,A_Q,h\nu) = TMR(z,A_Q,h\nu)\frac{SF(A_Q,h\nu)}{SF(0,h\nu)} - TMR(z,0,h\nu), \tag{6.61}$$

where $SF(A_Q,h\nu)$ and $SF(0,h\nu)$ are the scatter factors for fields A_Q and 0, respectively, and photon energy $h\nu$, as defined in Eq. (6.29).

The ratio $SF(A_Q,h\nu)/SF(0,h\nu)$ is then:

$$\frac{SF(A_Q,h\nu)}{SF(0,h\nu)}=\frac{\dfrac{PSF(A_Q,h\nu)}{PSF(10,h\nu)}}{\dfrac{PSF(0,h\nu)}{PSF(10,h\nu)}}=PSF(A_Q,h\nu) \tag{6.62}$$

since $PSF(0,h\nu)=1$.

For cobalt-60 gamma rays, *SMR*s are approximately the same as the *SAR*s. However, for megavoltage photon energies above cobalt-60 the *SMR*s should be calculated from *TMR*s using Eq. (6.61) and

$$TMR(z,0,h\nu)=e^{-\mu_{eff}(z-z_{\max})}, \tag{6.63}$$

where μ_{eff} is the effective attenuation coefficient for the photon beam $h\nu$.

6.9. OFF-AXIS RATIOS AND BEAM PROFILES

Dose distributions along the beam central axis give only part of the information required for an accurate dose description inside the patient. Dose distributions in 2-dimensions and 3-dimensions are determined with central axis data in conjunction with off-axis dose profiles.

In the simplest form, the off-axis data are given with beam profiles measured perpendicularly to the beam central axis at a given depth in phantom. The depths of measurement are typically at z_{max} and 10 cm for verification of compliance with machine specifications, in addition to other depths required by the particular treatment planning system. An example of typical dose profiles measured at various depths in water for two field sizes (10×10 and 30×30 cm^2) and a 10 MV x-ray beam is shown in Fig. 6.17.

Combining a central axis dose distribution with off-axis data results in a volume dose matrix that provides 2-D and 3-D information of the dose distribution. The off-axis ratio (OAR) is usually defined as the ratio of dose at an off-axis point to the dose on the central beam axis at the same depth in phantom.

Megavoltage x-ray beam profiles consist of three distinct regions: central region, penumbra and umbra.

- The central region represents the central portion of the profile extending from the beam central axis to within 1 cm to 1.5 cm from the geometric field edges of the beam. The geometrical field size, indicated by the optical light field, is usually defined as the separation between the 50% dose level points on the beam profile. In the central region, the beam profile for cobalt-60 beams is affected by the inverse-square dose falloff as well as by increased phantom thickness for off-axis points. For linacs, on the other hand, the central region of the beam profile is affected by the energy of electrons striking the thick target, by the target atomic number, and by the flattening filter atomic number and geometric shape.

- In the penumbral region of the dose profile the dose changes rapidly and depends also on the field defining collimators, the finite size of the focal spot (source size) and the lateral electronic dis-equilibrium. The dose fall-off around the geometrical beam edge is sigmoid in shape and extends under the collimator jaws into the penumbral tail region where there is a small component of dose due to transmission through the collimator jaws (*transmission penumbra*), a component attributed to finite source size (*geometric penumbra*), and a significant component due to inpatient x-ray scatter (*scatter penumbra*). The total penumbra is referred to as the *physical penumbra* and is a sum of the three individual penumbras: transmission, geometric and scatter. The physical penumbra depends on beam energy, source size, source-surface distance, source-collimator distance, and depth in phantom.

- Umbra is the region outside the radiation field, far removed from the field edges. The dose in this region is generally low and results from radiation transmitted through the collimator and head shielding.

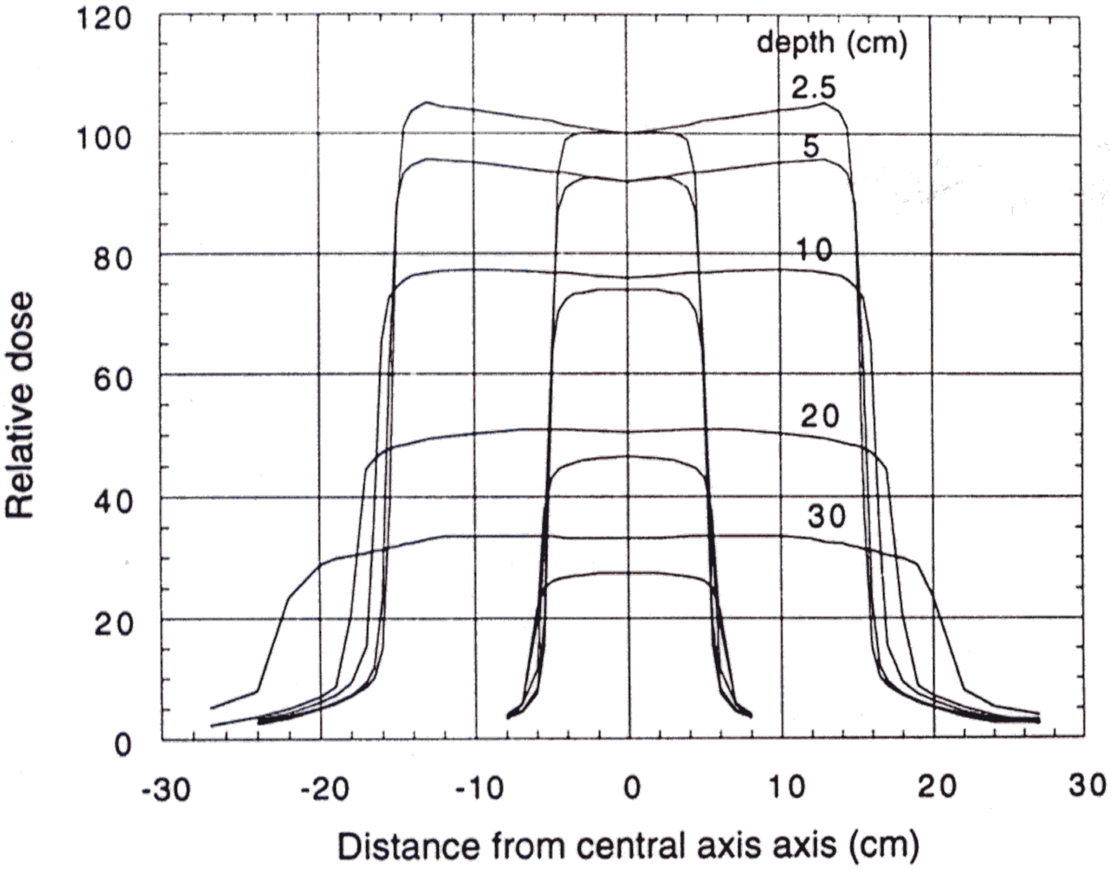

FIG. 6.17. An example of beam profiles for two field sizes (10× 10 cm^2 and 30× 30 cm^2) and a 10 MV x-ray beam at various depths in water. The central axis dose values are scaled by the appropriate PDD value for the two fields.

Dose profile uniformity is usually measured by a scan along the center of both major beam axes for various depths in the water phantom. Two parameters that quantify field uniformity are then determined: *field flatness* and *field symmetry*.

Beam flatness F is assessed by finding the maximum D_{max} and minimum D_{min} dose point values on the profile within the 80% of the beam width and then using the relationship:

$$F = 100 \times \frac{D_{\max} - D_{\min}}{D_{\max} + D_{\min}}. \tag{6.64}$$

Standard linac specifications generally require that $F < 3$ % when measured in a water phantom at a depth of 10 cm and an *SSD* of 100 cm for the largest field size available (usually $40 \times 40\ \text{cm}^2$).

Complying with the flatness specifications at a depth of 10 cm in water results in "over-flattening" at $z_{\max}$ that manifests itself in the form of "horns" in the profile, and "under-flattening" that progressively worsens as the depth z increases from 10 cm to larger depths beyond 10 cm, as evident from the profiles for the $30 \times 30\ \text{cm}^2$ field in Fig. 6.17. The "over-flattening" and "under-flattening" is caused by the lower beam effective energies in off-axis directions compared to the central axis direction.

Beam symmetry S is usually determined at z_{max} which represents the most sensitive depth for assessment of this beam uniformity parameter. Areas under the z_{max} beam profile on each side (left and right) of the central axis extending to the 50% dose level (normalized to 100% at the central axis point) are determined and S is then calculated from:

$$S = 100 \times \frac{(area_{\text{left}} - area_{\text{right}})}{(area_{\text{left}} + area_{\text{right}})} \ . \tag{6.65}$$

The areas under the $z_{\max}$ profiles can often be determined using an automatic option on the water tank scanning device (3-D isodose plotter). Alternately, using a planimeter or even counting squares on graph paper with a hard copy of the profile is an option.

6.10. ISODOSE DISTRIBUTIONS IN WATER PHANTOMS

Physical characteristics of radiation beams are usually measured in phantoms under standard conditions that are:

- *Homogeneous, unit density phantom*;
- *Flat phantom surface*;
- *Perpendicular beam incidence onto the phantom.*

The central axis depth dose data in conjunction with dose profiles contain complete 2D and 3D information about a radiation beam. However, this information is difficult to visualize even for a single beam, let alone for a combination of several beams. Therefore, planar and volumetric variations in depth doses are usually displayed by means of isodose curves or isodose surfaces, which connect points of equal dose in a volume of interest. The isodose curves and surfaces are usually drawn at regular intervals of absorbed dose and expressed as a percentage of the dose at a specific reference point.

An isodose chart for a given beam consists of a family of isodose curves usually drawn at regular increments of percent depth dose. Two normalization conventions are in use:

- For *SSD* setups, all isodose values are normalized to 100 at point *P* on the central axis,
- For *SAD* setups, the isodose values are normalized to 100 at the isocenter.

The isodose charts for an *SSD* setup are thus plots of *PDD* values, while isodose charts for an *SAD* setup are plots of either *TAR* or *TMR* values.

For a cobalt-60 beam the dose at any depth is the largest on the central beam axis and then decreases toward the beam edges. For megavoltage photon beams the off-axis dose at shallow depths is usually larger than the central axis dose at same depth as a consequence of flattening filter design. These filters provide flat beams at depth of 10 cm in water and to achieve this they must overcompensate at shallow depths. (Note: the effective beam energy in extreme off-axis directions is lower than the effective beam energy in the direction of the central beam axis).

Figure 6.18 shows an example of isodose charts for a cobalt-60 beam in water: part (a) for an *SSD* setup ($A = 10\times 10$ cm^2; $SSD = 80$ cm) and part (b) for an *SAD* setup ($A_Q = 10\times 10$ cm^2; *SAD* = 100 cm; depth of isocenter = 10 cm).

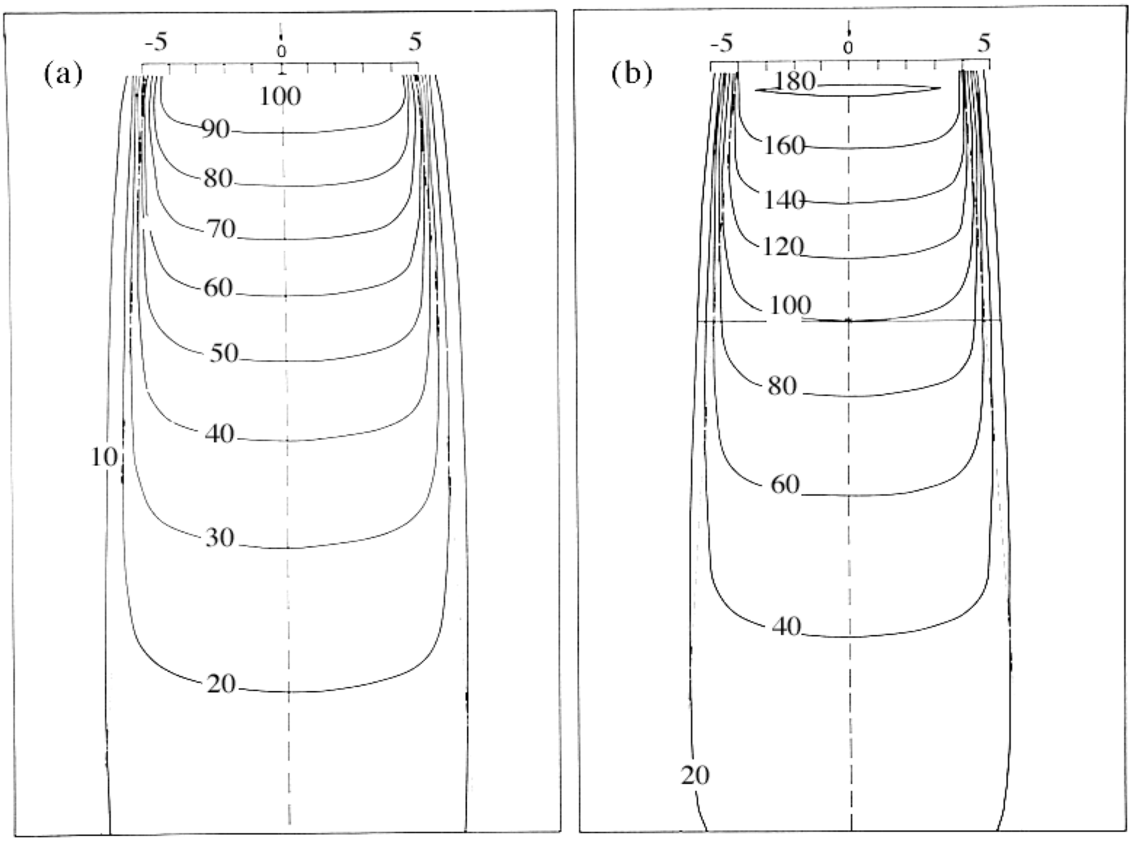

FIG. 6.18. Isodose curves for a cobalt-60 gamma ray beam: (a) for an SSD setup (A = 10×10 cm^2; SSD = 80 *cm) and (b) for an SAD setup (A$_Q$=10×10 cm^2, SAD =* 100 *cm; depth of isocenter is 10 cm).*

- Near the beam edges in the penumbra region the dose decreases rapidly with lateral distance from the beam central axis. This dose fall off is caused not only by the geometric penumbra but also by the reduced side scatter.

- Outside the geometric limits of the beam and the penumbra, the dose variation is the result of three components:

  (1) Scatter from the radiation field;
  (2) Leakage through the collimator jaws and machine head housing;
  (3) Scatter from the collimation system.

- Parameters that affect the single beam isodose distribution are beam quality, source size, beam collimation, field size, *SSD*, and the source-collimator distance.

- Isodose charts are measured with ionisation chambers, solid state detectors, standard radiographic film, and radiochromic film.

- In addition to direct measurements, isodose charts may also be generated by calculations using various algorithms for treatment planning, most commonly with commercially available treatment planning systems.

- Treatment by a single photon beam is seldom used except for superficial tumours. Deep-seated tumours are usually treated with a combination of two or more beams to achieve an acceptable dose distribution within the tumour and the surrounding normal tissues. As a rule, the tumour dose is higher than the dose to the surrounding normal tissues, and the dose distribution within the tumour should be homogeneous to within 7% and –5% of the prescribed dose, if at all possible.

6.11. ISODOSE DISTRIBUTIONS IN PATIENTS

In clinical situations the beam may be obliquely incident onto the patient and the patient surface may be curved or of irregular shape, requiring corrections for contour irregularities. In addition, some irradiated tissues, such as lung and bone, have densities that differ considerably from that of water, requiring corrections for tissue heterogeneities.

Isodose distributions in patients are determined by one of two radically different approaches:

(1) *correction-based algorithms*;
(2) *model-based algorithms.*

The *correction-based algorithms* use depth dose data measured in water phantoms with flat surface and normal incidence in conjunction with various methods to correct for irregular patient contours and oblique beam incidence in contrast to the flat surface of a water phantom). They also correct for *organ inhomogeneities* to account for varying electron densities of organs in contrast to the uniform electron density of a water phantom.

The *model-based algorithms* obviate the correction problem by modeling the dose distributions from first principles and accounting for all geometrical and physical characteristics of the particular patient treatment.

Before clinical use both the correction algorithms as well as model-based algorithms must be verified experimentally and this often represents a difficult task. The relative importance of individual corrections varies with particular treatment geometry and the position of the target volume inside the patient. For conventional treatment techniques the correction-based algorithms work reasonably well and produce reliable dose distributions; however, for the new sophisticated treatments such as 3D conformal radiotherapy and intensity-modulated radiotherapy (IMRT), they become problematic, because of the radical corrections that are required for these techniques. The model-based algorithms hold great promise for the future; however, they are currently still under development.

6.11.1. Corrections for irregular contours and oblique beam incidence

A radiation beam striking an irregular or sloping patient surface produces an isodose distribution that differs from the standard distributions obtained on flat surfaces with a normal beam incidence. Two approaches are used to address this problem:

(1) The effect can be corrected through various calculation methods
(2) The effect may be compensated for through the use of wedges, bolus materials or compensators.

Several methods were developed to correct standard flat surface/normal incidence isodose distributions for contour irregularities and oblique angles of beam incidence. The three most commonly used methods, applicable for angles of incidence up to 45° for megavoltage x-ray beams and up to 30° for orthovoltage x-ray beams, are:

(1) *Effective SSD method,*
(2) *TAR or TMR method*,
(3) *Isodose shift method.*

The correction factors for the three methods can be understood with reference to Fig. 6.19 where an irregular patient contour *CC* is treated with a beam with an *SSD = f.* The percentage depth dose at point *S* normalized to dose at point *P* on the beam central axis is referred to as PDD_{corr} and calculated with one of the three methods listed above.

In the ***effective SSD method***, PDD_{corr} is determined from:

$$PDD_{corr} = PDD'(z, A, f, h\nu) \left[\frac{f + z_{\max}}{f + h + z_{\max}} \right]^2 , \tag{6.66}$$

where *PPD'(z,A,f, hν)* is the percentage depth dose under standard conditions with the flat surface *C'C'* and the second term represents an inverse square correction factor. The parameter *h* is the thickness of missing tissue while the parameter *–h* represents the thickness of excess tissue. An assumption is made that the percentage depth dose does not depend on *SSD* for deviations from the nominal *SSD* on the order of *h*, *i.e.*, $h \ll f$. The resulting percentage depth dose is normalized to 100 at point *P* on the central beam axis.

Thus, in the effective *SSD* method: (i) the isodose chart is shifted to the flat surface level at the *C'C'* contour; (ii) the *PDD* value for point *X* is read; and (iii) the reading is corrected by an inverse-square law factor.

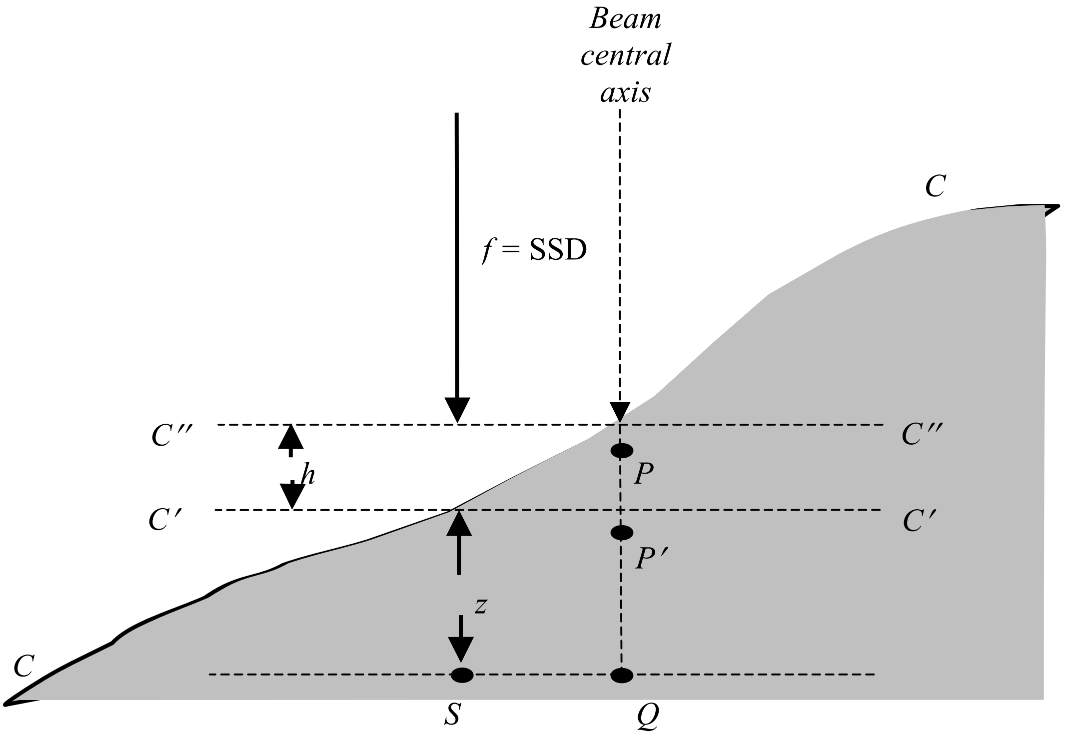

FIG. 6.19. Geometry used for dose determination at point S in a patient. CC represents the actual patient contour; C'C' and C"C" are flat phantom contours: C"C" at the nominal SSD and C'C' at SSD + h, where h represents the thickness of missing tissue directly above point S. Point P is the point of dose normalization at $z_{\max}$ on the central beam axis.

In the ***TAR or TMR method***, PDD_{corr} is given as:

$$PDD_{corr} = PDD''(z+h, A, f, h\nu)\ \frac{T(z, A_Q, h\nu)}{T(z+h, A_Q, h\nu)}, \tag{6.67}$$

where

A_Q	is the field size at point *X* at a distance (*f*+*z*+*h*) from the source,
T	stands for either the *TAR* or the *TMR*, and an assumption is made that the *TAR*s and *TMR*s do not depend on the *SSD*
PDD''	represents the percentage depth dose value at depth *(d+h)* for standard flat phantom with the surface at *C*"*C*".
h	is missing or excessive tissue. For missing tissue *h* is positive, for excess tissue *h* is negative.

In the ***isodose shift method***, the value of the dose at *X* is shifted on a vertical ray line by *(k×h)* where *h* is the thickness of the missing or excess tissue and *k* is a factor depending on beam energy. The factor *k* is smaller than 1, and has a value of 0.7 for cobalt-60 beams through 5 MV beams; 0.6 for 5-15 MV; and 0.5 for 15-30 MV beams. For missing tissue *h* is positive and the isodose is shifted away from the source, while for excess tissue *h* is negative and the isodose is shifted toward the source.

6.11.2. Missing tissue compensation

In addition to calculation techniques to correct for contour irregularities and oblique beam incidence, discussed in Section 6.11.1, many relatively simple techniques have been devised to compensate for missing tissue, most notably the use of wedges, bolus materials, and compensators.

Wedge filters may be used to even out the isodose surfaces for photon beams striking relatively flat patient surfaces under an oblique beam incidence. Two types of wedge filters are in use: (1) physical and (2) dynamic.

- Physical wedges are made of lead, brass or steel. When placed into a beam, they cause a progressive decrease in the intensity across the beam and a tilt of isodose curves under normal beam incidence.
- Dynamic wedges provide the wedge effect on isodose curves through a closing motion of a collimator block during irradiation.
- The wedge angle is defined as the angle through which an isodose curve at a given depth in water (usually 10 cm) is tilted at the central beam axis under the condition of normal beam incidence.
- Physical wedges are usually available with wedge angles of 15^o, 30^o, 45^o, and 60^o; the dynamic wedges are available with any arbitrary wedge angle in the range from 0^o and 60^o.
- The wedge (transmission) factor is defined as the ratio of doses at $z_{\max}$ in a water phantom on the beam central axis with and without the wedge.
- Physical wedge filters may alter the photon beam quality (beam hardening or beam softening), however, the effects are usually ignored, since their influence on dosimetric functions are minimal at depths smaller than 10 cm.

Bolus is a tissue-equivalent material placed directly on the skin surface to even out the irregular patient contour and thereby provide a flat surface for normal beam incidence. In principle, the use of bolus is straightforward and practical, however, it suffers a serious drawback: for megavoltage photon beams it results in the loss of the skin sparing effect in the skin under the bolus layer (skin sparing occurs in the bolus).

Compensators are used to produce the same effect as the bolus yet preserve the skin sparing effect of megavoltage photon beams. They are custom-made devices that mimic the shape of bolus but are placed into the radiation beam at some 15 to 20 cm from the skin surface so as not to disrupt the skin sparing properties of the beam. Although compensators may be made of water-equivalent materials, they are usually fabricated from lead or special low melting point alloys, such as cerrobend.

Since compensators are placed away from the skin surface, their shape must be adjusted for:

- Beam divergence;
- Linear attenuation coefficients of the compensator material relative to that of water;
- Reduction in scatter at various depths when the compensator is placed into the radiation beam away from the skin surface rather than in contact with the skin.

6.11.3. Corrections for tissue inhomogeneities

Standard isodose charts and depth dose tables are given for uniform density water phantoms. Radiation beams used in patient treatment, however, traverse various tissues that may differ in density and atomic number from water. These tissue inhomogeneities (also referred to as heterogeneities) affect the dose deposition in the patient and may result in isodose distributions that differ considerably from those obtained in water phantoms. The effects of inhomogeneities on radiation dose distributions depend on the amount, density and atomic number of the inhomogeneity as well as on the quality of the photon beam, and may be separated into two distinct categories:

- Increase or decrease in the attenuation of the primary beam that affects the distribution of the scattered radiation
- Increase or decrease of the secondary electron fluence

Three separate regions, in addition to inhomogeneity boundaries, are considered with regard to inhomogeneities: (1) point-of-interest *P* in front of the inhomogeneity; (2) *P* inside the inhomogeneity; and (3) *P* beyond the inhomogeneity.

In region (1) in front of the inhomogeneity, especially for megavoltage photons, the dose is not affected by the inhomogeneity, since the primary beam in this region is not affected and neither is the scatter component, except close to the boundary.

In region (2) the dose is mainly affected by changes in the secondary electron fluence and to a lesser extent by changes in the primary beam attenuation in the inhomogeneity. Under the conditions of electronic equilibrium and for a given photon energy fluence, the ratio of absorbed doses in two different media is equal to the ratio of mass energy absorption coefficients for the two media. Close to the soft tissue – lung interfaces there may be a partial loss of electronic equilibrium and an associated decrease in dose.

In region (3) beyond the inhomogeneity the dose is mainly affected by changes in the primary beam attenuation and to a lesser extent by changes in scatter. Four empirical methods (see Section 7.5.6) are available for correcting the water phantom dose to estimate the dose at points in region (3):

(1) *TAR method*
(2) *Power law TAR method*
(3) *Equivalent TAR method*
(4) *Isodose shift method*

Beyond healthy lung (density 0.3 g/cm^3) the dose in soft tissues will increase, while beyond bone (density 1.6 g/cm^3) it will decrease in comparison with uniform phantom dose.

- Typical corrections for dose beyond healthy lung are: 4%, 3%, 2%, and 1% per cm of lung for cobalt-60 gammas, 4 MV, 10 MV, and 20 MV x rays, respectively.
- The shielding effect of bone depends strongly on beam energy and is appreciable at low x-ray energies because of a strong photoelectric effect presence and essentially negligible in the low megavoltage energy range (mainly Compton effect). At energies above 10 MeV the shielding effect of bone begins to increase with increasing energy because of the increase in pair production cross section.

6.11.4. Model-based algorithms

Three groups of computational model-based algorithms fall into the category of model-based algorithms:

(1) A relatively simple *analytical calculation of first-order Compton scatter* and its addition to primary dose at point-of-interest. The method is fairly rudimentary and assumes a parallel beam of mono-energetic photons and ignores heterogeneities and scattering higher than the first order.

(2) The *convolution-superposition method* accounts for the indirect nature of dose deposition from photon interactions, separating the primary photon interactions from the transport of scattered photons and charged particles produced through photoelectric effect (photoeffect), Compton scattering and pair production.

(3) The *Monte Carlo method*, the most promising of the model-based dose computation methods, uses well-established probability distributions governing the individual interactions of photons and electrons with the patient and their transport through the patient. The Monte Carlo simulation is essential in all model-based dose computations to characterize the clinical beam emanating from the radiation source, but can also be used directly to compute photon dose distributions for a given patient and treatment geometry. The current limitation of direct Monte Carlo calculations is the time used to calculate the large number of histories required to reduce stochastic or random uncertainties to acceptable levels. It is expected that the advances in computer technology will, within a few years, reduce the Monte Carlo calculation times to acceptable levels and this will make Monte Carlo methods the standard approach to radiotherapy treatment planning.

6.12. CLARKSON SEGMENTAL INTEGRATION

Tables for the various dose functions, such as the percentage depth dose *PDD*, tissue-air ratio *TAR*, peak-scatter factor *PSF*, tissue-maximum ratio *TMR*, etc., are usually given for a series of square fields. Values for these functions when fields are rectangular or circular may be obtained through determining the equivalent square for the rectangular field [Eq. (7.25)] or circular field [Eq. (6.26)] and then using the appropriate tabulated square field data for determining the value of a given dose function. Here, an assumption is made that there is a match between dose functions for rectangular fields and their equivalent square fields and equivalent circular fields. It has been shown experimentally that this assumption is valid for the range of field sizes and beam energies used in radiotherapy.

Radiation fields other than square, rectangular or circular are termed irregular fields. An irregular field too will have an equivalent square field and an equivalent circular field that will yield the same value of a given dose function as does the irregular field, but there are no simple means to determine the equivalent square or equivalent circle for a given irregular field. However, a technique, referred to as the Clarkson segmental integration, can be used to calculate the appropriate value of any given dose function for the given irregular field based on circular field data.

- The Clarkson technique resolves the irregular field into sectors of circular beams originating at the point of interest *Q* in the phantom or patient. For manual calculations, sectors with an angular width of 10° are usually used, for computer-driven calculations the angular width is 5° or even smaller to improve accuracy.

- An assumption is made that a sector with a given field radius contributes $1/N$ of the total circular field value to the value of the given function *F* for the irregular field at point *Q* where *N* is the number of sectors in a full circle of 360°.

- The value of a given function *F* for an irregular field that in general depends on depth *d* of point *Q*, shape of the irregular field, source-surface distance *f*, and beam energy $h\nu$ is then determined from the following segmental integration relationship:

$$F(z, irreg. field, f, h\nu) = \frac{1}{N}\sum_{i=1}^{N} F(z, r_i, f, h\nu)\,, \tag{6.68}$$

where

N is the number of sectors in 360° (for manual calculations $N = 36$),
r_{i} is the radius from point *Q* to the edge of the field at the center of sector i, and
$F(z, r_{\mathrm{i}}, f, h\nu)$ is the value of the dosimetric function *F* at depth *z*, source-surface distance *f*, and beam energy $h\nu$ for the circular field with radius r_{i}.

An example of an irregular field is shown in Fig. 6.20 with two of 36 sectors highlighted: one is a simple sector with radius r_1 and the other is composite sector with three radii: r_{a}, r_{b} and r_{c}.

- The contribution of the simple sector to the sum in Eq. (6.68) is simply equal to $(1/N)\,F(z, r_{\mathrm{i}}, f, h\nu)$.

- The composite sector consists of three components to yield the following contribution $(1/N)\left[F(z, r_a, f, h\nu) - F(z, r_b, f, h\nu) + F(z, r_c, f, h\nu)\right]$ to the sum of Eq. (6.68) with two positive components that are contributed by portions of the radiation field and one negative component that accounts for the missing portion of the radiation field in the segment (sector).

Once the value of a dose function for a given irregular field is determined through the Clarkson integration technique, the equivalent square for the irregular field is also established by finding in tabulated square field data the square field that will give the same value for the dose function. Originally, the segmental integration technique was proposed by Clarkson in the 1940s and developed by Johns and Cunningham in the 1960s for determining the scatter component of the dose at an arbitrary point of interest in the patient either inside or outside the direct radiation field.

For points inside the radiation field the scatter component is added to the primary beam component, for points outside the field the scatter component is added to the radiation transmitted through the shielding blocks, collimator, or head shielding of the treatment machine.

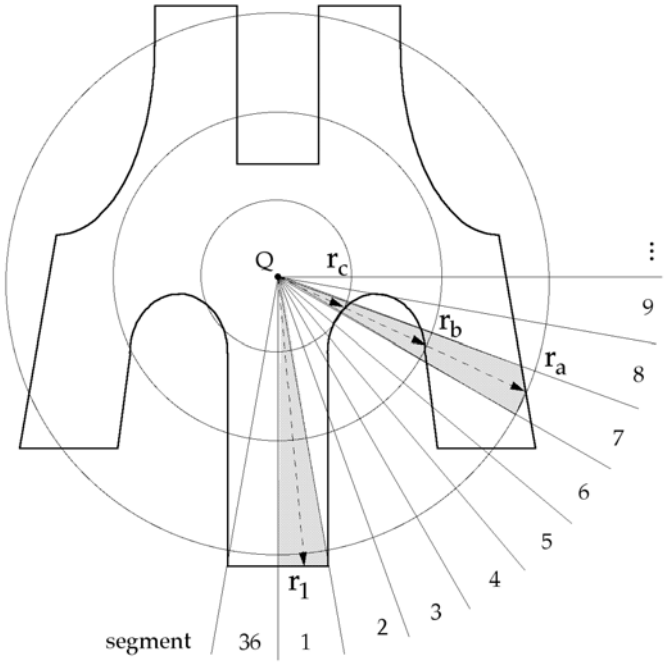

FIG. 6.20. An example of a mantle irregular field. Two segments out of 36 are highlighted. The first is simple with radius r_1, the seventh is composite with three radii: r_a, r_b, and r_c.

The original implementation of the Clarkson technique was intended for use with orthovoltage and cobalt beams for which the primary dose rate was reasonably flat from the central axis to points near the edge of the field where it began to decrease. In linac beams, however, the primary dose rate at shallow depths in the patient may actually increase at distances away from the central axis ("horns") as a result of flattening filter effects on the radiation beam. A flattening filter correction that depends on depth d in phantom and radial distance r from the central axis is required to model, for the primary beam component, this increase in the dose rate away from the central beam axis.

6.13. RELATIVE DOSE MEASUREMENTS WITH IONISATION CHAMBERS

Ionisation chambers are used in clinical physics not only for photon and electron beam calibration at a reference point in phantom but also for relative measurements of various parameters and dose functions such as collimator factor, relative dose factor, dose profiles, and percentage depth doses including the surface dose and doses in the build up region. The dependence of various dose correction factors (such as ionisation chamber polarity, ionic recombination, stopping power ratios and fluence correction) on beam energy, *i.e.*, depth in phantom, should be considered in relative dose measurements, although in many situations the dependence may be ignored.

Usually each task of dose determination is carried out with ionisation chambers designed for the specific task at hand. For example:

- Doses and dose rates at reference points in phantom for megavoltage photon beams and electron beams above 10 MeV are measured with relatively large volume (0.6 cm^3) cylindrical ionisation chambers in order to obtain a reasonable signal and good signal-to-noise ratio.

- Relative dose distributions (for example, central axis percentage depth doses and beam profiles) for photon beams beyond $z_{\max}$ and for electron beams are usually measured with small volume (0.1 cm^3) ionisation chambers in order to obtain good spatial resolution.

- Surface doses and doses in the build up region for photon beams are measured with parallel-plate ionisation chambers incorporating a thin polarizing electrode window (to be able to measure surface dose) and a small electrode separation (typically 1 mm for better spatial resolution).

- A typical megavoltage photon beam percentage depth dose (*PDD*) curve, measured with positive and negative polarities with a parallel-plate ionisation chamber in the dose build-up region and beyond, is sketched in Fig. 6.21.

- In the build-up region the positive chamber polarity produces a larger signal than the negative polarity. The difference in signals is most pronounced on the phantom surface and then diminishes with depth until it disappears at depths of $z_{\max}$ and beyond. At $z_{\max}$ and beyond this curve is more conveniently measured with small volume cylindrical ionisation chambers and the results will match those obtained with a parallel-plate chamber. In the build-up region, however, the cylindrical chamber will read an unrealistically high signal because of its excessive wall thickness.

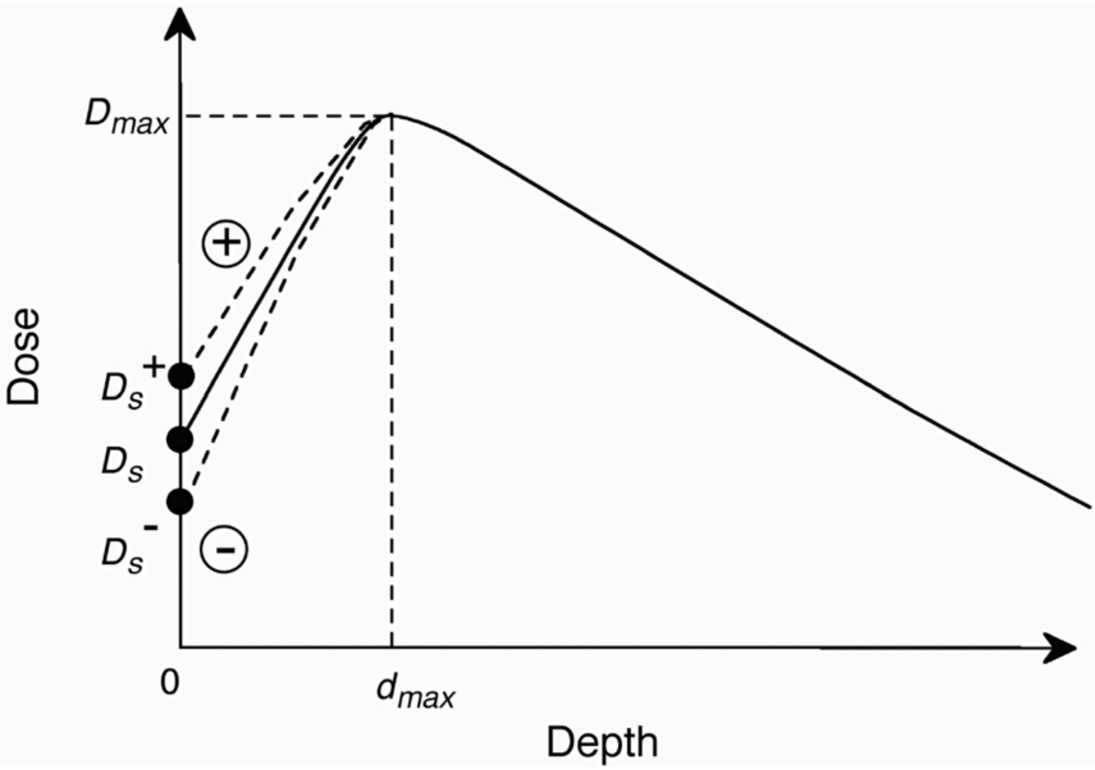

FIG. 6.21. Megavoltage photon beam depth doses measured with a parallel-plate ionisation chamber. In the build-up region the positive polarity produces a higher reading than the negative polarity, beyond $z_{\max}$ both polarities give essentially identical signals.

- In the build-up region, signals for both positive and negative chamber polarities are measured with a parallel-plate ionisation chamber and the average reading between the two polarities is used as the true dose value. The signal averaging eliminates the chamber *"Compton current"* that results from photon interactions in the chamber measuring electrode. In the build-up region, these interactions cause a loss of electrons from the measuring electrode which is not fully compensated by arrival of electrons from the upper layers of the phantom. The electron difference results in a non-dosimetric current, which is referred to as the "Compton current", and causes an increased reading for positive chamber polarity and a decreased reading for negative chamber polarity.

- For depths beyond $z_{\max}$, both positive and negative chamber polarities yield the same reading because electronic equilibrium exists on the measuring electrode (as many electrons land on the measuring electrode as are ejected by photon interactions from the measuring electrode).

- Ionic collection efficiency depends not only on the potential difference between the polarizing and measuring electrode but also on the dose rate in the ionisation chamber cavity. Therefore, in principle, when measuring depth doses, one should account for the change in ionic collection efficiency as a function of depth in phantom. However, in practice, since ionic recombination loss in well-behaved chambers is 2% or less, the changes in ionic recombination with depth are ignored when measuring relative depth doses.

- In general, stopping-power ratios water-to-air and chamber correction factors are also depth-dependent and this effect, depending on the particular situation and accuracy required, might have to be accounted for when measuring depth doses with ionisation chambers.

    - In *photon beams*, since the restricted stopping power ratio water-to-air is essentially independent of depth at depths larger than $z_{\max}$, the signal corrected for polarity effect can be treated as an indication of the relative dose-to-water. At depths shallower than $z_{\max}$, the restricted stopping power ratio water-to-air varies by up to 2% depending on field size and energy; a variation that is usually ignored.
    - In *electron beams*, the restricted stopping power ratio water-to-air varies significantly as a function of depth requiring a correction to the measured ionisation curve when relative dose is to be determined. For realistic beams as a function of depth z and energy (parametrized by R_{50}) the stopping power ratio water-to-air is given by following fit (Burns *et al.*, Med. Phys. **23**, 383; 1996):

$$\left(\frac{\bar{L}}{\rho}\right)_{\text{air}}^{\text{water}}(z,R_{50})=\frac{\mathrm{a}+\mathrm{b}(\ln R_{50})+\mathrm{c}(\ln R_{50})^2+d(z/R_{50})}{1+\mathrm{e}(\ln R_{50})+\mathrm{f}(\ln R_{50})^2+\mathrm{g}(\ln R_{50})^3+\mathrm{h}(z/R_{50})}, \qquad (6.69)$$

with the following values for the parameters:
a = 1.0752; b = -0.50867; c = 0.088670; d = -0.08402; e = -0.42806;
f = 0.064627; g = 0.003085; and h = -0.12460.

- Finally, in electron beams, for unguarded chambers (such as Farmer type thimble chambers), the fluence perturbation correction factor also varies as a function of energy at depth (by up to 5% in the range between $z_{\max}$ and the bremsstrahlung tail for a 20 MeV electron beam). Therefore, well-guarded parallel-plate ionisation chambers compared to thimble chambers are better suited for measurement of relative depth doses in electron beams.

6.14. DELIVERY OF DOSE WITH A SINGLE EXTERNAL BEAM

- Outputs for x-ray machines and isotope units are usually given in centigray per minute (cGy/min) at $z_{\max}$ in phantom, while outputs for linacs are given in centigray per monitor unit (cGy/MU) at $z_{\max}$ in phantom.

- Transmission ionisation chambers in linacs are usually adjusted such that beam output corresponds to 1 cGy/MU at $z_{\max}$ for a $10 \times 10\ \text{cm}^2$ field at *SSD* = 100 cm, *i.e.*, $\dot{D}_P(z_{\max}, 10, 100, h\nu) =$ 1 cGy/MU (Fig. 6.9).

- $\dot{D}_P(z_{\max}, A, 100, h\nu)$, the dose rate at point *P* for an arbitrary field size *A,* is then obtained from $\dot{D}_\mathrm{P}(z_{\max}, 10, 100, h\nu)$ as follows (see Eq. (6.30)):

$$\dot{D}_P(z_{\max}, A, 100, h\nu) = \dot{D}_P(z_{\max}, 10, 100, h\nu) \times RDF(A, h\nu) \quad . \qquad (6.70)$$

- The number of monitor units $\mathcal{MU}$ (in MUs)required to deliver a tumour dose *TD* at point *Q* (Fig. 6.9) using a single *SSD* field with field *A* is calculated from Eq. (6.34) recognizing that $\dot{D}_Q = \dot{TD} = (TD)/(\mathcal{MU})$ where $\dot{TD}$ is the tumour dose rate:

$$\mathcal{MU} = \frac{TD}{\dot{D}_P(z_{\max}, 10, 100, h\nu) \times RDF(A, h\nu) \times PDD(z, A, f, h\nu)} \quad . \qquad (6.71)$$

- Similarly, for an SAD set-up (Fig. 6.15) the number of monitor units $\mathcal{MU}$ to deliver a tumour dose *TD* at point *Q* with a single isocentric beam with field size *A* may be calculated using Eq. (6.52) recognizing that $\dot{D}_Q = \dot{TD} = (TD)/(\mathcal{MU})$ and that $\dot{D}_{Q_{\max}}(z_{\max}, A_Q, SAD = 100, h\nu)$ may be approximated as: (6.72)

$$\dot{D}_{Q_{\max}}(z_{\max}, A_Q, 100_{SAD}, h\nu) \approx \dot{D}_P(z_{\max}, 10, 100_{SSD}, h\nu) \times RDF(A, h\nu) \times \left(\frac{f + z_{ref}}{f} \right)^2$$

to get:

$$\mathcal{MU} = \frac{TD}{\dot{D}_P(z_{\max}, 10, 100_{SSD}, h\nu) \times RDF(A, h\nu) \times TPR(z, A_Q, h\nu)} \times \left(\frac{f}{f + z_{ref}} \right)^2 \qquad (6.73)$$

6.15. EXAMPLE OF DOSE CALCULATION

Given $\dot{D}(15,15,80,\mathrm{Co})$ calculate $\dot{D}(10,20,140,\mathrm{Co})$, where $\dot{D}(15,15,80,\mathrm{Co}) = \dot{D}(z,A,f,\mathrm{Co})$ stands for the dose rate in cGy/min at point Q in a water phantom at a depth $z = 15$ cm on the central axis of a cobalt beam with a field size $A = 15\times 15$ cm^2 and source-surface distance $SSD = f = 80$ cm.

The problem ties together the various basic functions and parameters that are routinely used in external beam radiotherapy and may be solved using either the *SSD* approach (with percentage depth doses) or the *SAD* approach (with tissue-air ratios). The two approaches, of course, should yield the same end result. The steps involved in going from $\dot{D}(15,15,80,Co)$ to $\dot{D}(10,20,140,Co)$ are given below for the *SSD* and the *SAD* approaches.

SSD approach (6.74)

$$\begin{array}{l}
\dot{D}(15,15,80,\mathrm{Co}) \\
\downarrow \quad \times\dfrac{1}{PDD(15{,}15{,}80{,}\mathrm{Co})} \\
\dot{D}(0.5,15,80,\mathrm{Co}) \\
\downarrow \quad \times\dfrac{1}{PSF(15{,}\mathrm{Co})} \\
\dot{D}'_{80.5}(15_{80,}\mathrm{Co}) \\
\downarrow \quad \times\dfrac{CF(11.4{,}\mathrm{Co})}{CF(15{,}\mathrm{Co})} \\
\dot{D}'_{80.5}(11.4_{80},\mathrm{Co}) \\
\downarrow \quad \times\dfrac{80.5^2}{140.5^2} \\
\dot{D}'_{140.5}(20_{140},\mathrm{Co}) \\
\downarrow \quad \times PSF(20{,}\mathrm{Co}) \\
\dot{D}(0.5,20,140{,}\mathrm{Co}) \\
\downarrow \quad \times PDD(10{,}20{,}140{,}\mathrm{Co}) \\
\dot{D}(10,20,140,\mathrm{Co}),
\end{array}$$

SAD approach (6.75)

$$\begin{array}{l}
\dot{D}(15,15,80,\mathrm{Co}) \\
\downarrow \quad \times\dfrac{1}{TAR(15{,}17.8{,}\mathrm{Co})} \\
\dot{D}'_{95}(17.8,\mathrm{Co}) \\
\downarrow \quad \times\dfrac{95^2}{80.5^2} \\
\dot{D}'_{80.5}(15_{80,}\mathrm{Co}) \\
\downarrow \quad \times\dfrac{CF(11.4{,}\mathrm{Co})}{CF(15,\mathrm{Co})} \\
\dot{D}'_{80.5}(11.4_{80},\mathrm{Co}) \\
\downarrow \quad \times\dfrac{80.5^2}{150^2} \\
\dot{D}'_{150}(21.4_{150},\mathrm{Co}) \\
\downarrow \quad \times TAR(10{,}21.4{,}\mathrm{Co}) \\
\dot{D}(10,20,140{,}\mathrm{Co})
\end{array}$$

where $\dot{D}'_{140.5}(20_{140},\mathrm{Co})$ stands for "dose rate to small mass of water" at a distance of 140.5 cm from the source with the collimator set to give 20×20 cm^2 at 140 cm from the source corresponding to 11.4×11.4 cm^2 at 80 cm from the source.

The general answer for the ***SSD approach*** is:

$$\frac{\dot{D}(10,20,140,\mathrm{Co})}{\dot{D}(15,15,80,\mathrm{Co})}=\frac{PDD(10,20,140,\mathrm{Co})}{PDD(15,15,80,\mathrm{Co})}\times\frac{PSF(20,\mathrm{Co})}{PSF(15,\mathrm{Co})}\times\frac{CF(11.4,\mathrm{Co})}{CF(15,\mathrm{Co})}\times\frac{80.5^2}{140.5^2}=$$

$$=\frac{PDD(10,20,140,\mathrm{Co})}{PDD(15,15,80,\mathrm{Co})}\times\frac{RDF(20,\mathrm{Co})}{RDF(15,\mathrm{Co})}\times\frac{CF(11.4,\mathrm{Co})}{CF(20,\mathrm{Co})}\times\frac{80.5^2}{140.5^2} \tag{6.76}$$

The general answer for the ***SAD approach*** is:

$$\frac{\dot{D}(10,20,140,\mathrm{Co})}{\dot{D}(15,15,80,\mathrm{Co})}=\frac{TAR(10,21.4,\mathrm{Co})}{TAR(15,17.8,\mathrm{Co})}\times\frac{CF(11.4,\mathrm{Co})}{CF(15,\mathrm{Co})}\times\frac{95^2}{150^2} \tag{6.77}$$

Both answers with standard cobalt-60 machine data (see, for example, Brit. J. Radiol., Suppl. 25) will yield for the ratio of the two dose rates 0.505 within ±1%.

In Eq. (6.74) we get to $\dot{D}'_{80.5}(11.4,\mathrm{Co})$ from $\dot{D}(0.5,15,80,\mathrm{Co})$ following a path that leads through $\dot{D}'_{80.5}(15_{80},\mathrm{Co})$ as follows:

$$\dot{D}'_{80.5}(11.4,\mathrm{Co})=\dot{D}(0.5,15,80,\mathrm{Co})\times\frac{1}{PSF(15,\mathrm{Co})}\times\frac{CF(11.4,\mathrm{Co})}{CF(15,\mathrm{Co})}. \tag{6.78}$$

We can also attain $\dot{D}'_{80.5}(11.4,\mathrm{Co})$ by going in phantom from $\dot{D}(0.5,15,80,\mathrm{Co})$ to $\dot{D}(0.5,11.4,80,\mathrm{Co})$ and then to $\dot{D}'_{80.5}(11.4_{80},\mathrm{Co})$ as follows:

$$\begin{array}{l}\dot{D}(0.5,15,80,\mathrm{Co})\\ \downarrow\quad\times\dfrac{RDF(11.4,\mathrm{Co})}{RDF(15,\mathrm{Co})}\\ \dot{D}(0.5,11.4,80,\mathrm{Co})\\ \downarrow\quad\times\dfrac{1}{PSF(11.4,\mathrm{Co})}\\ \dot{D}'_{80.5}(11.4_{80},\mathrm{Co})\end{array} \tag{6.79}$$

Both paths, of course, will give identical end results, since, as can be shown using Equations (6.29) and (6.31):

$$\frac{1}{PSF(15,\mathrm{Co})}\times\frac{CF(11.4,\mathrm{Co})}{CF(15,\mathrm{Co})}=\frac{RDF(11.4,\mathrm{Co})}{RDF(15,\mathrm{Co})}\times\frac{1}{PSF(11.4,\mathrm{Co})}. \tag{6.80}$$

6.16. SHUTTER CORRECTION TIME

In radiotherapy machines that use an electrical timer for measuring the dose delivery (radiotherapy x-ray machines and teletherapy isotope machines) account must be taken of possible end-effects (*shutter correction time*) resulting from switching the beam ON and OFF. In x-ray machines the beam output builds up from zero to its full value as the generating voltage builds up in the first few seconds of the treatment. In isotope machines the source is moved into position at the start of treatment and returned to its safe position at the end of treatment.

The *shutter correction time* τ is defined as the time that must be added to or subtracted from the calculated treatment time T_c to deliver accurately the prescribed dose to the patient. For a given therapy machine the shutter correction time is typically determined by measuring two doses (D_1 and D_n) at a given point P (for example, at z_{max} in phantom):

- D_1 is measured with a relatively long exposure time T (on the order of 5 minutes), contains one end-effect, and is given by: $D_1 = \dot{D}(T+\tau)$ or $\dot{D} = D_1/(T+\tau)$.
- D_n is measured cumulatively with n dose segments, each having an exposure time T/n. The dose D_n thus contains n end-effects, the cumulative beam-on time is again equal to T, and D_n is given by: $D_n = \dot{D}(T+n\tau)$ or $\dot{D} = D_n/(T+n\tau)$.

Solving for τ the equation for the true dose rate $\dot{D} = D_1/(T+\tau) = D_n/(T+n\tau)$ results in the following expression for the shutter correction time:

$$\tau = (D_n - D_1)T/(nD_1 - D_n). \tag{6.81}$$

In Eq. (6.81) $\tau > 0$ for $D_n > D_1$; $\tau = 0$ for $D_n = D_1$; and $\tau < 0$ for $D_n < D_1$. The time set on the timer will be $(T_c - \tau)$. Typical shutter correction times are of the order of 1 second.

BIBLIOGRAPHY

BURNS, D.T., DING, G.X., ROGERS, D.W.O., "R_{50} as beam quality specifier for selecting stopping power ratios and reference depths for electrons", Med. Phys. **23**, 383-388 (1996).

BRITISH JOURNAL OF RADIOLOGY, Supplement 25, "Central Axis Depth Dose Data for Use in Radiotherapy: 1996", British Institute of Radiology, London, U.K. (1996).

HENDEE, W.R., IBBOTT, G.S., "Radiation therapy physics", Mosby-Yearbook, St. Louis, Missouri, U.S.A. (1996).

JOHNS, H.E., CUNNINGHAM, J.R., "The physics of radiology", Thomas, Springfield, Illinois, U.S.A. (1984).

KHAN, F.M., "The physics of radiation therapy", Williams and Wilkins, Baltimore, Maryland, U.S.A. (1994).

WILLIAMS, J.R., THWAITES, D.I. (editors), "Radiotherapy physics in practice", Oxford University Press, Oxford, United Kingdom (2000).